

Infrared Emission from Interstellar Dust. IV. The Silicate-Graphite-PAH Model in the Post-Spitzer Era

B.T. Draine

Princeton University Observatory, Peyton Hall, Princeton, NJ 08544;
draine@astro.princeton.edu

and

Aigen Li

Department of Physics and Astronomy, University of Missouri, Columbia, MO 65211;
LiA@missouri.edu

ABSTRACT

Infrared (IR) emission spectra are calculated for dust heated by starlight, for mixtures of amorphous silicate and graphitic grains, including varying amounts of polycyclic aromatic hydrocarbon (PAH) particles. The models are constrained to reproduce the average Milky Way extinction curve.

The calculations include the effects of single-photon heating. Updated IR absorption properties for the PAHs are presented, that are consistent with observed emission spectra, including those newly obtained by *Spitzer Space Telescope*. We find a size distribution for the PAHs giving emission band ratios consistent with the observed spectra of the Milky Way and other galaxies.

Emission spectra are presented for a wide range of starlight intensities. We calculate how the efficiency of emission into different IR bands depends on PAH size; the strong $7.7\ \mu\text{m}$ emission feature is produced mainly by PAH particles containing $< 10^3$ C atoms. We also calculate how the emission spectrum depends on U , the starlight intensity relative to the local interstellar radiation field. The submm and far-infrared emission is compared to the observed emission from the local interstellar medium.

Using a simple distribution function, we calculate the emission spectrum for dust heated by a distribution of starlight intensities, such as occurs within galaxies. The models are parameterized by the PAH mass fraction q_{PAH} , the lower cutoff U_{min} of the starlight intensity distribution, and the fraction γ of the dust heated by starlight with $U > U_{\text{min}}$. We present graphical procedures using Spitzer IRAC and MIPS photometry to estimate the parameters q_{PAH} , U_{min} , and γ , the fraction f_{PDR} of the dust luminosity coming from photodissociation regions with $U > 100$, and the total dust mass M_{dust} .

Subject headings: radiation mechanisms: thermal; ISM: dust, extinction; infrared: galaxies; infrared: ISM

1. Introduction

Interstellar dust in galaxies absorbs energy from starlight; this absorbed energy is then reradiated at infrared (IR) and far-IR wavelengths. The unprecedented sensitivity of Spitzer Space Telescope (Werner et al. 2004a) allows this IR emission to be measured for a wide range of galaxy sizes and morphologies. The spectral properties of the IR emission from dust allow one to infer the composition of the dust, the size distribution of the dust particles, the intensity of the starlight that is heating the dust, and the total mass of dust.

Deducing the dust properties and starlight intensity is by no means direct or straightforward. To start, one needs to assume a provisional dust model with the physical nature of the dust (composition, geometry, and size distribution) fully specified. One then tries to constrain the grain properties by comparing model predictions with observations (e.g. interstellar extinction, scattering, polarization, IR and microwave emission, and interstellar depletions).

Various models have been proposed for interstellar dust. The models fall into three broad categories: the silicate-graphite model (Mathis et al. 1977; Draine & Lee 1984; Kim et al. 1994) and its natural extension – the silicate-graphite-PAH model (Siebenmorgen & Krügel 1992; Li & Draine 2001a; Weingartner & Draine 2001a); the silicate core-carbonaceous mantle model (Desert et al. 1990; Jones et al. 1990; Li & Greenberg 1997), and the composite model which assumes the dust to be low-density aggregates of small silicates and carbonaceous particles (Mathis & Whiffen 1989; Mathis 1996; Zubko et al. 2004). The core-mantle model is challenged by the nondetection of the $3.4\ \mu\text{m}$ C–H aliphatic hydrocarbon polarization on sightlines where the $9.7\ \mu\text{m}$ Si–O silicate band is observed to be polarized (Chiar et al. 2006; Mason et al. 2006) [see also Adamson et al. (1999); Li & Greenberg (2002)]. The original composite model proposed by Mathis & Whiffen (1989), with $\sim 80\%$ of the grain volume consisting of vacuum, may have too flat a far-IR emissivity to explain the observational data (Draine 1994). The updated version of the composite model of Mathis (1996) assumes a vacuum fraction $\sim 45\%$ in order to make economical use of the available carbon to account for the observed extinction while satisfying the “subsolar” interstellar abundance budget suggested by Snow & Witt (1996). However, Dwek (1997) argues that this dust model emits too much in the far-IR in comparison with observations. The latest version of the composite model put forward by Zubko et al. (2004) aims at reproducing the observed interstellar extinction and IR emission within a “subsolar” abundance budget. The ability of composite grain models to reproduce the observed extinction within “subsolar” abundance constraints was recently challenged by Li (2005) based on

the Kramers-Kronig relations.¹

In this paper we calculate the IR emission expected from a specific physical model of interstellar dust – the silicate-graphite-PAH model. In this model, the dust is assumed to consist of a mixture of carbonaceous grains and amorphous silicate grains, with size distributions that are consistent with the observed wavelength-dependent extinction in the local Milky Way (Weingartner & Draine 2001a), including different amounts of polycyclic aromatic hydrocarbon (PAH) material.

Spectroscopic observations with *ISO* revealed the rich spectrum of PAHs (see, e.g., Beintema et al. (1996); Tielens et al. (1999); Joblin et al. (2000)). The model presented here posits “astro-PAH” absorption properties that are consistent with spectroscopic observations of PAH emission from dust in nearby galaxies (Smith et al. 2006). The model calculations show how the IR emission depends on the PAH abundance, and also on the intensity of starlight heating the dust. Comparison of models to infrared photometry obtained with *Spitzer Space Telescope* allows one to estimate PAH abundances, starlight intensities, and total dust masses.

The plan of this paper is as follows:

With new laboratory data [particularly the near-IR absorption spectra of PAH ions measured by Mattioda et al. (2005b)] and *Spitzer* spectroscopic data [with new PAH features discovered (Smith et al. 2004a; Werner et al. 2004b; Smith et al. 2006) and the familiar 7.7, 8.6, and 11.3 μm features resolved into several subfeatures (Smith et al. 2006) we update in §2 the cross sections $C_{\text{abs}}(\lambda)$ that we previously assumed for the PAH particles² (Li & Draine 2001a). We distinguish the PAHs by 2 charge states: either neutral (PAH^0) or ionized (PAH^\pm). We assume that multiply-charged (both positively and negatively) PAHs all have the same cross sections as those of singly-charged cations. The resulting “astro-PAH” absorption cross sections do not represent any specific material, but should approximate the actual absorption properties of the PAH mixture in interstellar space.

In §3 we show examples of temperature distribution functions for both neutral and ionized PAHs heated by starlight. These temperature distribution functions are then used to calculate emission spectra for individual particles in §4, which are in turn used to prepare a plot (Figure 6) showing how the efficiency of emitting into different emission features depends on the PAH size.

¹ Total (gas + dust) interstellar abundances remain uncertain. The most recent determination of the solar oxygen abundance $(\text{O}/\text{H})_\odot = 10^{-3.34 \pm 0.05}$ (Asplund et al. 2004) is close to the value for B stars in the Orion association $\text{O}/\text{H} = 10^{-3.31 \pm 0.03}$ (Cunha et al. 2006). The warm interstellar medium gas has $\text{O}/\text{H} = 10^{-3.41 \pm 0.01}$ (Cartledge et al. 2006), consistent with $\sim 20\%$ of the oxygen in silicate grains. For “refractory” elements such as Mg, Si, and Fe, however, partial separation of dust and gas by processes such as radiation pressure, ambipolar diffusion, and gravitational sedimentation in the process of star formation could result in stellar abundances differing from interstellar abundances (Snow 2000; Draine 2004). Photospheric abundances may therefore not be a reliable indicator of interstellar abundances for the elements that form refractory grains.

² Note that “PAH particles”, “PAH grains”, and “PAH molecules” are synonymous.

When we observe emission from a region in the Milky Way or another galaxy, there will always be a mixture of dust types and sizes present. We consider the emission from a specific set of dust mixtures, as described in §5. All the dust mixtures considered here are consistent with the observed “average” extinction curve for diffuse regions in the local Milky Way, but they differ from one another in the assumed abundance of small PAH particles. In §6 we show that the far-IR and submm emission calculated for the model is consistent with the COBE-FIRAS observations of emission from dust in the local Milky Way. In §7 we show that the calculated IRAC band ratios appear to be consistent with the spectrum of diffuse emission from the Milky Way, as determined by Flagey et al. (2006) from Spitzer Space Telescope observations.

The long wavelength emission from the dust model depends on the intensity of the starlight heating the dust. It will often be the case that the region observed (e.g., an entire star-forming galaxy) will include dust heated by a wide range of starlight intensities. In §8 we describe a simple parametric model for the distribution of the dust mass between regions with starlight intensities ranging from low to very high. We show in §9 how observations in the 3 MIPS bands ($24\ \mu\text{m}$, $71\ \mu\text{m}$, and $160\ \mu\text{m}$) plus the $3.6\ \mu\text{m}$ and $7.9\ \mu\text{m}$ IRAC bands³ can be used to estimate the parameters describing the distribution of starlight intensities as well as the fraction q_{PAH} of the total dust mass that is in PAHs, thereby allowing estimation of the total dust mass M_{dust} in the emitting region. A reader interested primarily in applying the results of this paper to interpretation of IRAC and MIPS observations may wish to proceed directly to §9.

The results of the paper are discussed in §10 and summarized in §11.

2. PAH Cross Sections: Post-Spitzer Era

The strong and ubiquitous interstellar emission features observed at $3.3\ \mu\text{m}$, $6.2\ \mu\text{m}$, $7.7\ \mu\text{m}$, $8.6\ \mu\text{m}$, and $11.3\ \mu\text{m}$ almost certainly arise from vibrational modes of polycyclic aromatic hydrocarbon (PAH) material, with C–H stretching modes producing the $3.3\ \mu\text{m}$ feature, C–H bending modes producing the in-plane $8.6\ \mu\text{m}$ and out-of-plane $11.3\ \mu\text{m}$ features, and C–C stretching and bending modes producing emission features at $6.2\ \mu\text{m}$, $7.7\ \mu\text{m}$, and longer wavelengths (Leger & Puget 1984; Allamandola et al. 1985).⁴

³ The IRAC and MIPS bands are often referred to using nominal wavelengths 3.6, 4.5, 5.8, 8.0, 24, 70, and $160\ \mu\text{m}$. However, to two significant digits, the effective wavelengths of IRAC bands 3 and 4 are $5.7\ \mu\text{m}$ and $7.9\ \mu\text{m}$ (IRAC Data Handbook Version 3.0), and that of MIPS band 2 is $71\ \mu\text{m}$ (MIPS Data Handbook Version 3.2) and we will use these wavelengths to refer to the bands.

⁴ Other carriers have also been proposed, including hydrogenated amorphous carbon (HAC) (Jones et al. 1990), quenched carbonaceous composite (QCC) (Sakata et al. 1987), coal (Papoular et al. 1993), hydrogenated fullerenes (Webster 1993), and nanodiamonds (Jones & d’Hendecourt 2000). The HAC, QCC, and coal hypotheses assume that the emission arises following photon absorption in small thermally-isolated aromatic units within or attached to these bulk materials (Duley & Williams 1981). However, it does not appear possible to confine the absorbed photon energy within these aromatic “islands” for the time $\gtrsim 10^{-3}\ \text{s}$ required for the thermal emission process (see

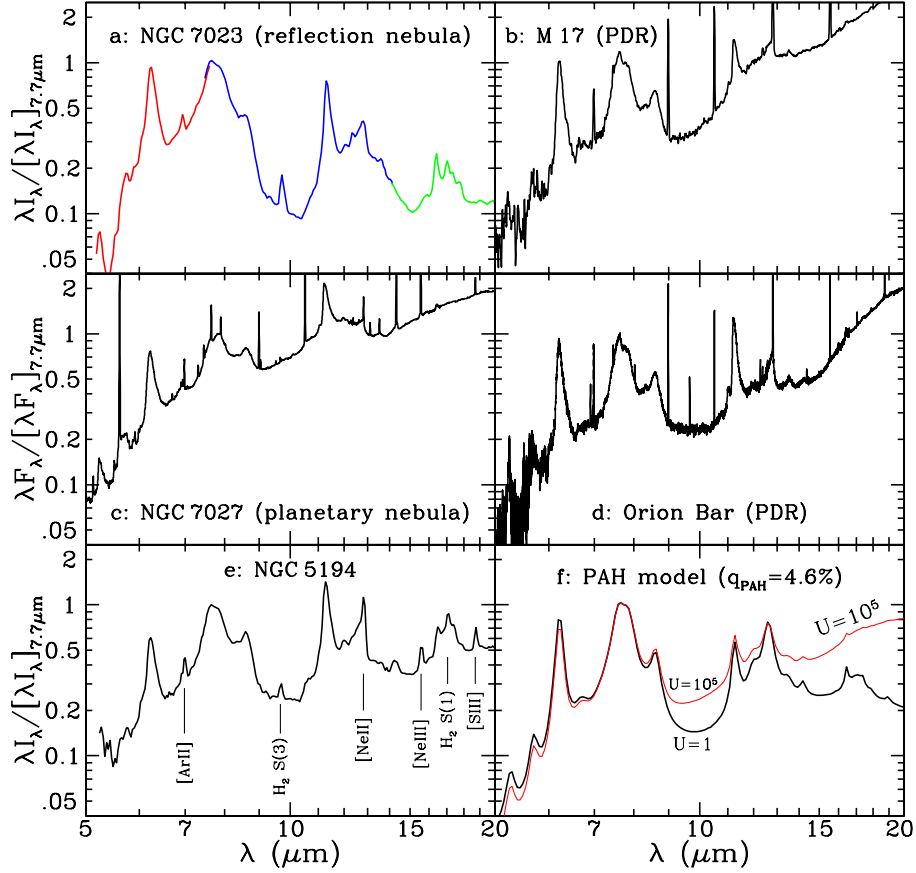


Fig. 1.— Observed 5–20 μm spectra for: (a) Reflection nebula NGC 7023 (Werner et al. 2004b); (b) Orion Bar PDR (Verstraete et al. 2001); (c) M17 PDR (Peeters et al. 2005); (d) Planetary nebula NGC 7027 (van Diedenhoven et al. 2004); (e) Seyfert Galaxy NGC 5194 (Smith et al. 2006). Also shown (f) is the emission calculated for the present dust model with $q_{\text{PAH}} = 4.6\%$, illuminated by the local diffuse starlight with $U = 1$ and 10^5 (see Fig. 13).

To reproduce this emission, a dust model must include a substantial population of ultrasmall grains or large molecules with the vibrational properties of PAH material and with sizes such that single-photon heating can excite the observed vibrational emission. Because the exact composition of the interstellar PAH material is unknown, and also because laboratory knowledge of the optical properties of PAHs is very limited, it is necessary to make assumptions regarding the absorption cross sections of the PAH particles.

The approach taken here to modeling the PAHs is to try to find optical properties for “astro-

Li & Draine (2002a)). Free-flying fullerenes and nanodiamonds have the required small heat capacity, but: (1) There are strong upper limits on the abundance of C_{60} and C_{60}^+ (Moutou et al. 1999); (2) Although not ruled out, there is little spectroscopic evidence for hydrogenated nanodiamond in the ISM.

Table 1: PAH Resonance Parameters.

j	λ_j (μm)	γ_j	$\sigma_{\text{int},j} \equiv \int \sigma_{\text{abs},j} d\lambda^{-1}$		tentative identification
			neutral (10^{-20}cm/C)	ionized (10^{-20}cm/C)	
1	0.0722	0.195	7.97×10^7	7.97×10^7	$\sigma \rightarrow \sigma^*$ transition in aromatic C
2	0.2175	0.217	1.23×10^7	1.23×10^7	$\pi \rightarrow \pi^*$ transition in aromatic C
3	1.050	0.055	0	2.0×10^4	weak electronic transition(s) in PAH cations
4	1.260	0.11	0	0.078	weak electronic transition(s) in PAH cations
5	1.905	0.09	0	-146.5	?
6	3.300	0.012	394(H/C)	89.4(H/C)	aromatic C-H stretch
7	5.270	0.034	2.5	20.	C-H bend + C-H stretch combination mode
8	5.700	0.035	4	32.	C-H bend + C-H stretch combination mode
9	6.220	0.030	29.4	235.	aromatic C-C stretch (in-plane)
10	6.690	0.070	7.35	59.	?
11	7.417	0.126	20.8	181.	aromatic C-C stretch
12	7.598	0.044	18.1	163.	aromatic C-C stretch
13	7.850	0.053	21.9	197.	C-C stretch + C-H bending
14	8.330	0.052	6.94(H/C)	48.(H/C)	C-C stretch + C-H bending?
15	8.610	0.039	27.8(H/C)	194.(H/C)	C-H in-plane bending
16	10.68	0.020	0.3(H/C)	0.3(H/C)	C-H out-of-plane bending, solo?
17	11.23	0.012	18.9(H/C)	17.7(H/C)	C-H out-of-plane bending, solo
18	11.33	0.032	52.(H/C)	49.(H/C)	C-H out-of-plane bending, solo
19	11.99	0.045	24.2(H/C)	20.5(H/C)	C-H out-of-plane bending, duo
20	12.62	0.042	35(H/C)	31(H/C)	C-H out-of-plane bending, trio
21	12.69	0.013	1.3(H/C)	1.3(H/C)	C-H out-of-plane bending, trio
22	13.48	0.040	8.0(H/C)	8.0(H/C)	C-H out-of-plane bending, quartet?
23	14.19	0.025	0.45	0.45	C-H out-of-plane bending, quartet?
24	15.90	0.020	0.04	0.04	?
25	16.45	0.014	0.5	0.5	C-C-C bending?
26	17.04	0.065	2.22	2.22	C-C-C bending?
27	17.375	0.012	0.11	0.11	C-C-C bending?
28	17.87	0.016	0.067	0.067	C-C-C bending?
29	18.92	0.10	0.10	0.17	C-C-C bending?
30	15	0.8	50.	50.	

PAH” material that appear to be physically reasonable (i.e., band strengths within the range measured for PAHs in the laboratory), in order to estimate the sizes and abundance of interstellar PAHs that would be consistent with the observed emission spectra. To this end, we adopt feature profiles that are based on astronomical observations. At wavelengths $\lambda > 5.5\mu\text{m}$, the spectra for the central regions of galaxies in the SINGS galaxy sample (Smith et al. 2006) provide observed profiles for the spectral features that the present model attempts to mimic. We follow Li & Draine (2001a) (hereafter LD01) in describing the PAH vibrational resonances by Drude profiles (components $j = 6\text{--}26$ in Table 1),⁵

⁵Boulanger et al. (1998) have shown that Lorentz profiles provide good fits to the PAH emission features from the

$$\Delta C_{\text{abs}}(\lambda) = N_{\text{C}} \sum_{j=1}^{25} \frac{2}{\pi} \frac{\gamma_j \lambda_j \sigma_{\text{int},j}}{(\lambda/\lambda_j - \lambda_j/\lambda)^2 + \gamma_j^2} \quad , \quad (1)$$

but with new profile parameters, adjusted to closely resemble the observed profiles. The profile parameters are given in Table 1, where λ_j , $\gamma_j \lambda_j$, and $\sigma_{\text{int}} \equiv \int \sigma_{\text{abs}} d\lambda^{-1}$ are, respectively, the peak wavelength, the FWHM, and the integrated strength per C atom of the j -th Drude resonance. The features in Table 1, and their identifications, have been discussed previously [see, e.g., Tielens (2005)], with Smith et al. (2006) providing a comprehensive study of the 5–35 μm emission from galaxies. We assume the PAH particles to have absorption cross sections per carbon atom $C_{\text{abs}}(\lambda)/N_{\text{C}}$ equal to those adopted by Li & Draine (2001a) [see eq. 5–11 of that paper] except for the following changes:

1. For PAH ions, we add additional absorption in the near-IR as recommended by Mattioda et al. (2005a). This consists of a “continuum” term

$$\frac{\Delta C_{\text{abs}}(\lambda)}{N_{\text{C}}} = 3.5 \times 10^{-19-1.45/x} \exp(-0.1x^2) \text{ cm}^2 \quad \text{for ions,} \quad x \equiv (\lambda/\mu\text{m})^{-1} \quad . \quad (2)$$

Because PAH ions were already assumed to absorb strongly at $\lambda \lesssim 0.8\mu\text{m}$, this additional absorption is numerically insignificant for $\lambda \lesssim 0.8\mu\text{m}$; the factor $\exp(-0.1x^2)$ has been added simply to force this term to go smoothly to zero as $\lambda \rightarrow 0$.

2. For PAH ions, we add near-IR resonances at wavelengths 1.05 μm and 1.26 μm plus a negative “resonance” term at 1.905 μm to suppress absorption in the 1.8–2.0 μm region, as recommended by Mattioda et al. (2005a); the three features are represented by Drude profiles, with parameters as given in Table 1. The negative term at $\lambda = 1.905\mu\text{m}$ ($j = 5$) was suggested by the recent laboratory data of Mattioda et al. (2005b). Removal of this term has a negligible effect on the heating or cooling rates of PAHs except in regions illuminated by very cool stars ($T_{\text{eff}} \lesssim 1500\text{ K}$) or in regions where the PAHs are excited to unusually high temperatures ($T \gtrsim 1500\text{ K}$).
3. Small changes have been made to central wavelengths and feature widths (e.g., $\lambda_j = 6.20\mu\text{m} \rightarrow 6.22\mu\text{m}$ and $\gamma_j = 0.032 \rightarrow 0.0284$ for the feature near 6.2 μm , $\lambda_j = 11.9\mu\text{m} \rightarrow 11.99\mu\text{m}$ and $\gamma_j = .025 \rightarrow 0.050$ for the feature near 12 μm , and $\lambda_j = 12.7\mu\text{m} \rightarrow 12.61\mu\text{m}$ and $\gamma_j = .024 \rightarrow 0.0435$ for the feature near 12.7 μm) guided by spectra obtained recently by *Spitzer Space Telescope* (Smith et al. 2006).
4. The integrated strength $\sigma_{\text{int}} \equiv \int \sigma_{\text{abs}} d\lambda$ of the 3.3 μm feature has been increased by a factor 1.5 for neutrals, and a factor 2 for ions, to better agree with the range of values calculated for a number of PAHs (see Figure 2).

NGC 7023 reflection nebula and the ρ Oph molecular cloud. The Drude profile closely resembles a Lorentz profile (both have more extended wings than a Gaussian profile). We favor the Drude profile as it is expected for classical damped harmonic oscillators.

5. σ_{int} for the $6.22\mu\text{m}$ feature is 50% of the value in LD01.
6. The $7.7\mu\text{m}$ complex is now composed of three components, at 7.417 , 7.598 , and $7.850\mu\text{m}$, with σ_{int} equal to 50% of the $7.7\mu\text{m}$ feature in LD01.
7. σ_{int} of the $8.6\mu\text{m}$ feature in LD01 is now shared by features at 8.330 and $8.610\mu\text{m}$, with σ_{int} equal to 50% of the $8.6\mu\text{m}$ feature in LD01.
8. The $11.3\mu\text{m}$ feature is now composed of features at 11.23 and $11.30\mu\text{m}$, with σ_{int} equal to 50% of the $11.3\mu\text{m}$ feature in LD01.
9. The integrated strength σ_{int} of the $12.7\mu\text{m}$ feature has been multiplied by 0.63 for both neutrals and ions relative to LD01.
10. Weak features have been added at $5.70\mu\text{m}$, $6.69\mu\text{m}$, $13.60\mu\text{m}$, $14.19\mu\text{m}$, $15.90\mu\text{m}$, and $18.92\mu\text{m}$, as seen in spectra of star-forming galaxies in the SINGS survey (Smith et al. 2006). The $5.70\mu\text{m}$ feature has previously been seen in planetary nebulae (Allamandola et al. 1989a) and PDRs (Verstraete et al. 1996; Peeters et al. 2004), and is presumed to be due to combination and overtone bands involving C-H out-of-plane bending modes.
11. A weak feature at $5.25\mu\text{m}$ seen in spectra of the M17 PDR and the Orion Bar (Verstraete et al. 1996; Peeters et al. 2004) and presumed to be due to C-H out-of-plane combination and overtone modes (Allamandola et al. 1989a), has been added.
12. The strength of the $16.4\mu\text{m}$ feature has been multiplied by 0.14 relative to LD01.
13. A new emission complex near $17\mu\text{m}$ has been added, composed of features at 17.038 , 17.377 , and $17.873\mu\text{m}$ (Smith et al. 2004a; Werner et al. 2004b; Smith et al. 2006).
14. Emission features at 21.2 and $23.1\mu\text{m}$ were seen in some laboratory samples (Moutou et al. 1996), and were therefore included by LD01 as examples of features that might be observed at $\lambda \gtrsim 20\mu\text{m}$. However, the SINGS spectra (Smith et al. 2006) do not show any features at $\lambda > 19\mu\text{m}$. The 21.2 and $23.1\mu\text{m}$ features have therefore been eliminated in the new model.
15. LD01 included a broad absorption component with $\lambda_j = 26\mu\text{m}$, $\gamma_j = 0.69$, and $\sigma_{\text{int}} = 18 \times 10^{-20} \text{ cm}^2/\text{C}$. This has been replaced by a broad absorption component with $\lambda_{27} = 15\mu\text{m}$, $\gamma_{27} = 0.8$, and $\sigma_{\text{int}} = 50 \times 10^{-20} \text{ cm}^2/\text{C}$ to provide continuum emission from $13\mu\text{m}$ longward.

In general, PAHs and larger grains will not be spherical, but we will characterize a grain of mass M by the effective radius a , defined to be the radius of an equal volume sphere: $a \equiv (3M/4\pi\rho)^{1/3}$, where amorphous silicate is assumed to have a mass density $\rho = 3.5 \text{ g cm}^{-3}$, and carbonaceous grains are assumed to have a mass density due to graphitic carbon alone of $\rho = 2.2 \text{ g cm}^{-3}$.

Thus the number of carbon atoms in a carbonaceous grain is

$$N_{\text{C}} = 460 \left(\frac{a}{10 \text{ \AA}} \right)^3 . \quad (3)$$

The smallest PAH considered in this paper has $N_C = 20$ C atoms (corresponding to $a \approx 3.55 \text{ \AA}$) since smaller PAHs are photolytically unstable (Allamandola et al. 1989b). As in LD01, we assume the number of H atoms per C atom to depend on the size of the PAH:

$$\begin{aligned}
 \text{H/C} &= 0.5 && \text{for } N_C \leq 25 \\
 &= 0.5 (25/N_C)^{1/2} && 25 \leq N_C \leq 100 \\
 &= 0.25 && N_C \geq 100
 \end{aligned} \tag{4}$$

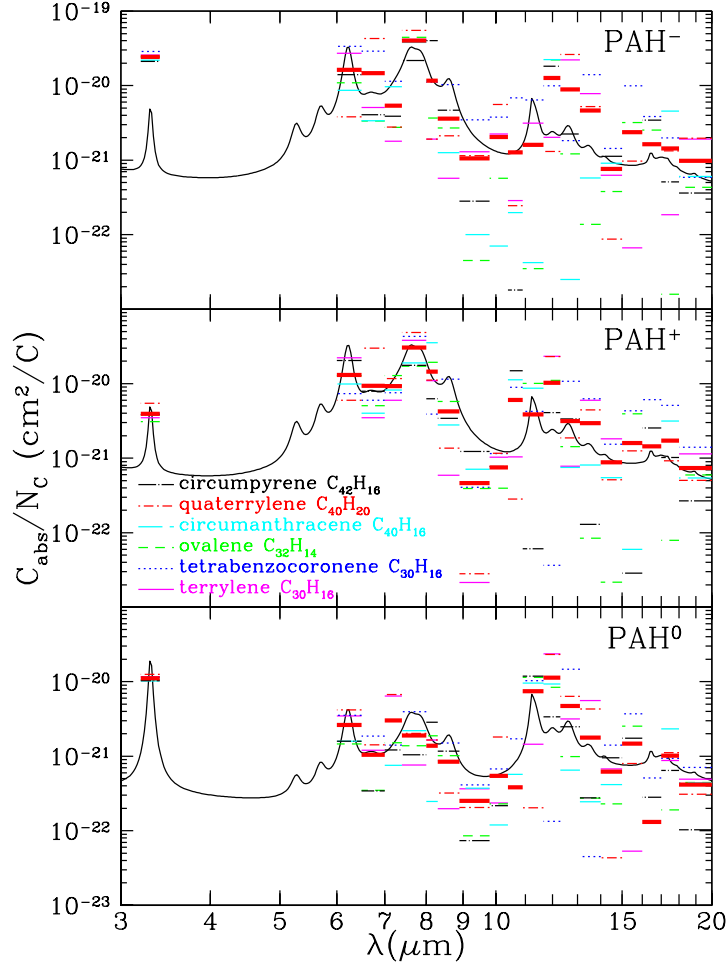


Fig. 2.— Solid curve: adopted absorption cross section per C from eq. (5) with $C/H \approx 3.2$ (e.g., $C_{64}H_{20}$). For the neutrals, anions, and cations listed in the figure legends, the horizontal line segments indicate the average absorption over that frequency intervals, taken from theoretical calculations by Mallocci et al. (2006). The heavy solid line segment is the average for the 6 species shown.

Figure 2 shows the adopted $C_{\text{abs}}(\lambda)$ in the infrared for a PAH molecule with $H/C=5/16$ (e.g., $C_{64}H_{20}$, with $a = 5.18 \text{ \AA}$). Also shown are values of C_{abs} per C atom, averaged over wavelength intervals, for a number of molecules for which C_{abs} has been calculated theoretically (Mallocci et al.

2006) for selected PAH molecules, cations, and anions. The first thing to note is the wide range of absorption cross sections per C. For example, in the case of the $3.3\ \mu\text{m}$ C–H stretch, the integrated absorption cross section per C varies by a factor of 25 among the PAH cations. The absorption averaged over the $7.5\text{--}8.0\ \mu\text{m}$ range varies by a factor of 30 among the neutral PAHs. Similar large variations in absorption cross sections are also seen at other wavelengths. Our adopted cross section falls within the range found for the sample of molecules shown in Fig. 2.

Figure 3 compares our adopted absorption cross sections for both neutral and ionized PAHs.

As in LD01, as the number N_{C} of carbon atoms in the grain increases, we assume a continuous change in optical properties from those of PAH material when N_{C} is small, to those of graphite when N_{C} is large. The transition from PAH to graphite is entirely ad-hoc: we take

$$C_{\text{abs}}(\lambda) = (1 - \xi_{\text{gra}}) C_{\text{abs}}(\text{PAH}, N_{\text{C}}) + \xi_{\text{gra}} C_{\text{abs}}(\text{graphite}, a) \quad (5)$$

where we take the graphite “weight” ξ_{gra} to be

$$\xi_{\text{gra}} = 0.01 \text{ for } a \leq 50 \text{ \AA} \quad (N_{\text{C}} \leq 5.75 \times 10^4) \quad (6)$$

$$= 0.01 + 0.99 \left[1 - \left(\frac{50 \text{ \AA}}{a} \right)^3 \right] \text{ for } a \geq 50 \text{ \AA} \quad (\text{i.e. } N_{\text{C}} \geq 5.75 \times 10^4) \quad (7)$$

The rationale for this is as follows: in addition to the C–H stretching mode emission at $3.3\ \mu\text{m}$, there appears to be $2\text{--}5\ \mu\text{m}$ continuum emission from the interstellar medium (Lu et al. 2003; Helou et al. 2004) and we therefore need a source of continuum opacity in the $2\text{--}5\ \mu\text{m}$ region that is not provided by the C–H and C–C stretching and bending modes. Here we assume that every small PAH has a small amount of “continuum” opacity, equal to 1% of what would have been calculated with the optical properties of bulk graphite (i.e. $\xi_{\text{gra}} = 0.01$). When the carbonaceous particles have $N_{\text{C}} \gtrsim 10^5$, they are assumed to behave like bulk graphite.

Graphite is highly anisotropic, with different dielectric functions ϵ_{\perp} and ϵ_{\parallel} for electric fields perpendicular and parallel to the “ c -axis” (the c -axis is normal to the “basal plane” of graphite). For $1\ \mu\text{m} < \lambda < 20\ \mu\text{m}$, absorption in small randomly-oriented graphite spheres is primarily due to the free electrons in graphite moving in the basal plane. However, the basal plane conductivity is large enough that at wavelengths $\lambda > 30\ \mu\text{m}$ the absorption is primarily due to the weak but nonzero conductivity parallel to the c -axis. The contribution of “free electrons” to ϵ_{\parallel} results in an absorption peak near $30\ \mu\text{m}$ (Draine & Lee 1984). This peak is seen for $a \geq 60\ \text{\AA}$ in Figure 3b. This absorption peak results in a broad emission feature near $30\ \mu\text{m}$ when the $a \gtrsim 60\ \text{\AA}$ graphite particles are heated to $T \gtrsim 100\ \text{K}$.

The peak in C_{abs} near $30\ \mu\text{m}$ in Figure 3b is a consequence of our adopted dielectric function for graphite, which is based on a simple “free electron” model that may not apply to realistic carbonaceous grains. For example, the measured absorption in amorphous carbon grains (Tanabe et al. 1983; Mennella et al. 1999) does not appear to show a peak near $30\ \mu\text{m}$. This is further discussed in §10.7

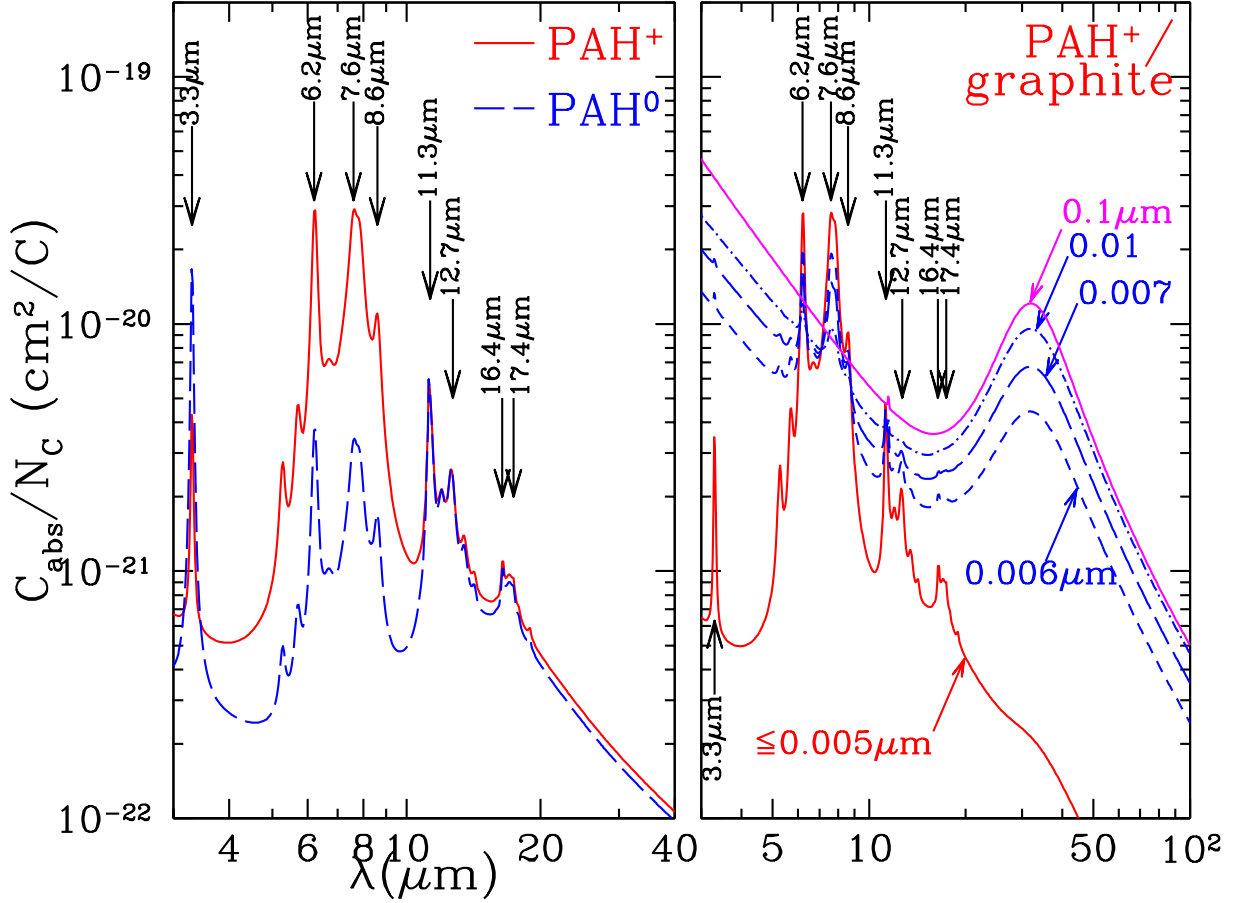


Fig. 3.— Absorption cross section per C atom for (a) neutral and ionized PAHs, and (b) for ionized carbonaceous grains, with properties of PAHs for $6 \text{ \AA} < a < 50 \text{ \AA}$, and properties of graphite spheres for $a \gtrsim 100 \text{ \AA}$. See §2 for details.

3. Heating of Dust by Starlight

We consider heating of grains by radiation with energy density per unit frequency

$$u_\nu = U \times u_\nu^{\text{MMP83}} \quad (8)$$

where U is a dimensionless scaling factor and u_ν^{MMP83} is interstellar radiation field (ISRF) estimated by Mathis et al. (1983)[hereafter MMP83] for the solar neighborhood.

For each grain composition and radius a , we use a detailed model for the heat capacity (Draine & Li 2001) to calculate the function $\bar{E}(T)$, the expectation value for the vibrational energy of the grain when in equilibrium with a heat reservoir at temperature T . For a grain with vibrational energy E , the grain “temperature” $T(E)$ is taken to be the temperature at which the expectation value for the vibrational energy would be E : $\bar{E}(T) = E$; we use this temperature estimate for all values of the vibrational energy E , in this respect departing from Draine & Li (2001),

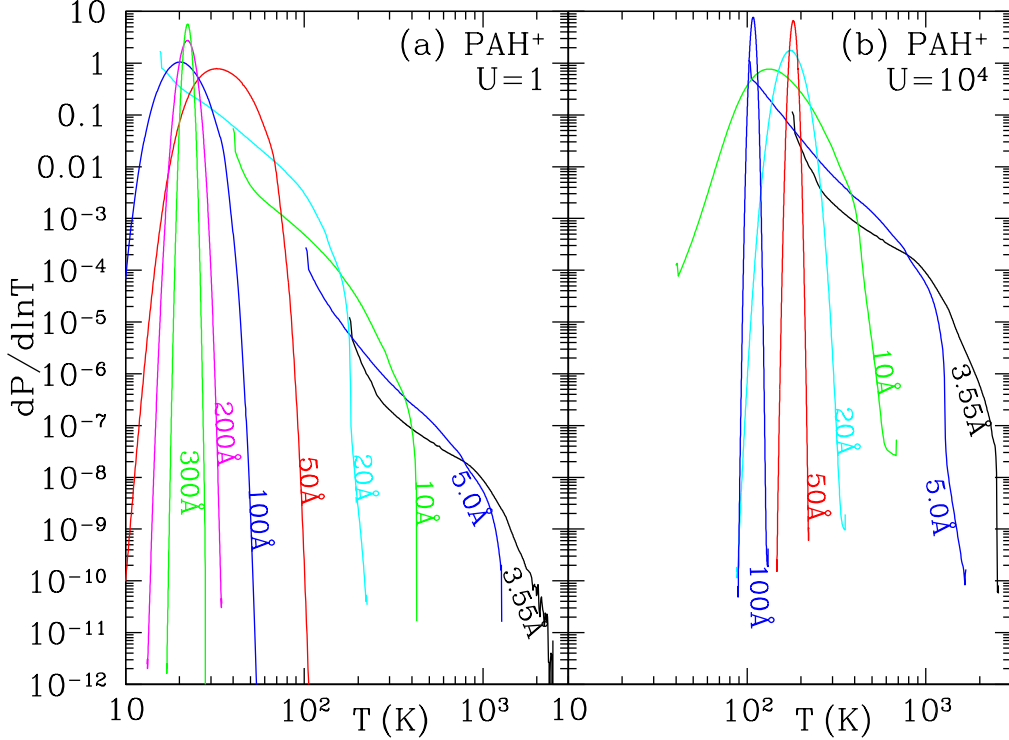


Fig. 4.— Temperature probability distribution $dP/d\ln T$ for selected carbonaceous grains heated by starlight with $U = 1$ and $U = 10^4$.

who used a different estimate for the temperature when dealing with the first 20 vibrational excited states. This does not appreciably affect the emission spectrum since almost all of the absorbed photon energy is reradiated while the grain is at high temperatures.

For each grain composition, radius a , and radiation intensity scale factor U , we determine the probability distribution function dP/dT , where dP is the probability of finding the grain with temperature in $[T, T + dT]$. For large grains, dP/dT is approximated by a delta function $dP/dT \approx \delta(T - T_{ss})$, where the “steady-state” temperature $T_{ss}(a)$ is the temperature at which the radiated power is equal to the time-averaged heating rate for a grain of radius a . For small grains, we find the steady-state solution dP/dT for grains subject to stochastic heating by photon absorption, and cooling by emission of infrared photons, using the “thermal-discrete” approximation (Draine & Li 2001), where the downward transition probabilities for a grain with vibrational energy E are estimated using a thermal approximation. For each grain size a and radiation intensity U , we divide the energy range $[E_{min}, E_{max}]$ into 500 bins. E_{min} and E_{max} are found iteratively, with the requirement that the probability of the grain being outside the range $[E_{min}, E_{max}]$ be negligible.

Figure 4 shows $dP/d\ln T$ for PAH⁺/graphite grains for selected grain sizes, for $U = 1$ and $U = 10^4$. In Figure 4a one sees that small grains undergo extreme temperature excursions (the $a = 3.55 \text{ \AA}$

PAH occasionally reaches $T > 2000$ K), whereas larger grains (e.g., $a = 300$ Å) have temperature distribution functions that are very strongly-peaked, corresponding to only small excursions around a “steady-state” temperature T_{ss} (the temperature for which the rate of radiative cooling would equal the time-averaged rate of energy absorption).

Figure 4b shows $dP/d\ln T$ for $U = 10^4$. It is apparent that when the rate of starlight heating is increased, the “steady-state” temperature approximation becomes valid for smaller grains. For example, for $U = 10^4$ one could approximate an $a = 50$ Å grain as having a steady temperature $T_{\text{ss}} \approx 150$ K whereas for $U = 1$ the temperature excursions are very important for this grain. The radius below which single photon heating is important, and above which the grain temperature can be approximated as being constant, is the size for which the time between photon absorptions becomes equal to the radiative cooling time (Draine & Li 2001). Or (equivalently), it is the size for which the thermal energy content of the grain when at T_{ss} is equal to the energy of the most energetic photons heating the grain.

4. Single-Grain Emission Spectra

From the probability distributions dP/dT , we calculate the time-averaged emission spectra for individual particles,

$$p_\lambda = \int 4\pi C_{\text{abs}}(\lambda) B_\lambda(T) \frac{dP}{dT} dT \quad , \quad (9)$$

$$B_\lambda(T) \equiv 2hc^2 \lambda^{-5} [\exp(hc/\lambda kT) - 1]^{-1} \quad . \quad (10)$$

Figure 5 shows the 3–30 μm emission from PAH ions and PAH neutrals heated by $U = 1$ starlight, with spectra shown for a number of different sizes. As expected, the short wavelength emission (e.g., the 3.3 μm feature) is strong only for the smallest particles, which can be heated to $T \gtrsim 10^3$ K by absorption of a single ultraviolet photon (see Fig. 4). As the particle size becomes larger, the short wavelength emission falls off, and an increasing fraction of the absorbed starlight energy is radiated in the longer wavelength modes. Emission in the 17 μm complex, for example, is most efficient for $a \approx 15$ Å.

The dependence of the feature emission on grain size is shown in Figure 6. From this plot it is apparent that emission in the 3.30 μm feature will be almost entirely due to $a \lesssim 6$ Å, or $N_{\text{C}} \lesssim 10^2$, whereas grains with radii as large as 12 Å, or $N_{\text{C}} \approx 10^3$, are efficient at converting absorbed starlight into 7.7 μm emission. The 11.3 μm feature can be produced by particles as large as $a \approx 20$ Å or $N_{\text{C}} \approx 4000$, and the 16.45 μm feature and 17.4 μm complex are efficiently produced by PAH particles in the 8–25 Å size range ($300 \lesssim N_{\text{C}} \lesssim 10^4$).

The PAH emission spectra shown in Figure 5 and the band emission efficiencies shown in Figure 6 are independent of the starlight intensity U in the single-photon-heating regime, $U \lesssim 10^4$ for $\lambda \lesssim 30 \mu\text{m}$. For larger grains, and at higher starlight intensities, the emission spectra do depend

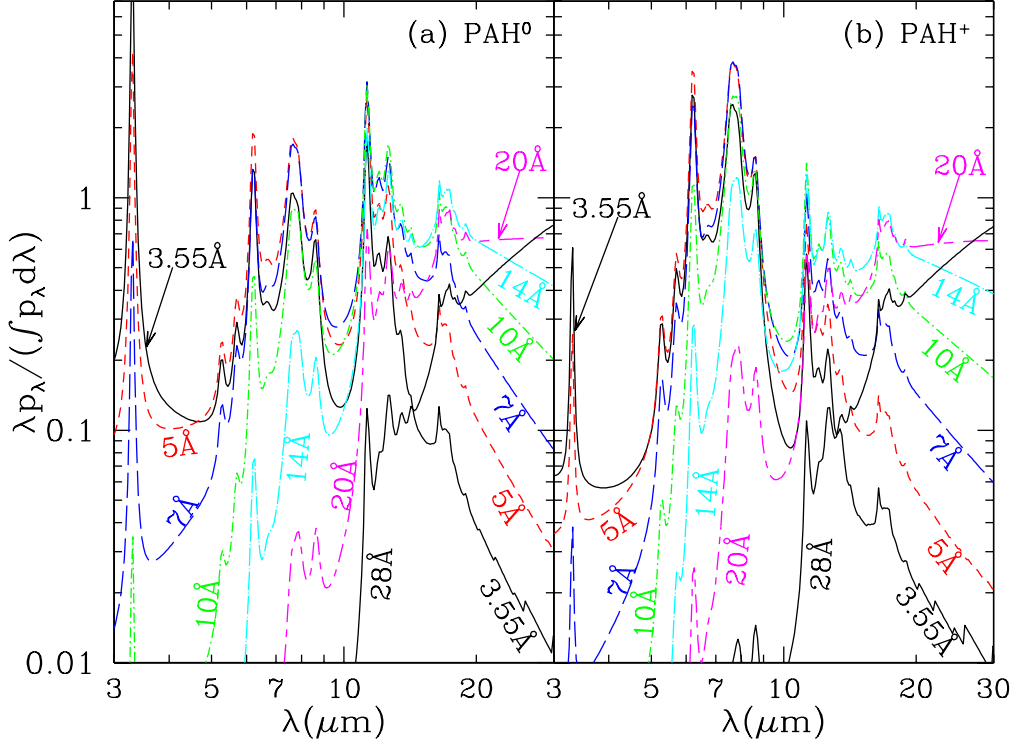


Fig. 5.— Normalized time-averaged emission spectra for $U < 10^4$ for (a) neutral and (b) ionized PAHs of various sizes (see text).

on U . If $C_{\text{abs}} \propto \lambda^{-2}$ for $\lambda \gtrsim 30 \mu\text{m}$, then the power radiated by the grain $\propto T^6$, the steady-state temperature $T_{\text{ss}} \propto U^{1/6}$, and the infrared emission will peak at a wavelength $\lambda_p \propto 1/T_{\text{ss}} \propto U^{-1/6}$.

The PAHs in the interstellar medium will consist of a mixture of neutral and ionized particles. For a given size PAH, the ionization balance will depend on the gas temperature, the electron density, and the ultraviolet radiation field (Weingartner & Draine 2001b). Here we adopt the ionization balance estimated by Li & Draine (2001a) for the diffuse ISM in the Milky Way – a weighted sum of the ionization fractions calculated for PAHs in the CNM (cold neutral medium), WNM (warm neutral medium) and WIM (warm ionized medium). For this weighted sum of neutral and ionized PAHs, $\lambda p_\lambda/p$ at selected wavelengths is shown as a function of grain size in Figure 7. Note that most of the selected wavelengths coincide with the positions of PAH emission features, thus indicating how PAH size affects the efficiency of converting starlight energy into IR emission features. The adopted ionization fraction as a function of grain size is shown in Figure 8.

Figure 7 also shows $\lambda p_\lambda/p$ evaluated at the $23.7 \mu\text{m}$ wavelength of the MIPS $24 \mu\text{m}$ band. We see that PAHs in the $15\text{--}40 \text{Å}$ size range ($2000 \lesssim N_C \lesssim 3 \times 10^4$) are relatively efficient at converting starlight energy into $24 \mu\text{m}$ continuum following single-photon heating (Figure 4 shows that a single $h\nu < 13.6 \text{eV}$ photon can heat a 20Å PAH to $\sim 170 \text{K}$). The term “very small grains” is sometimes

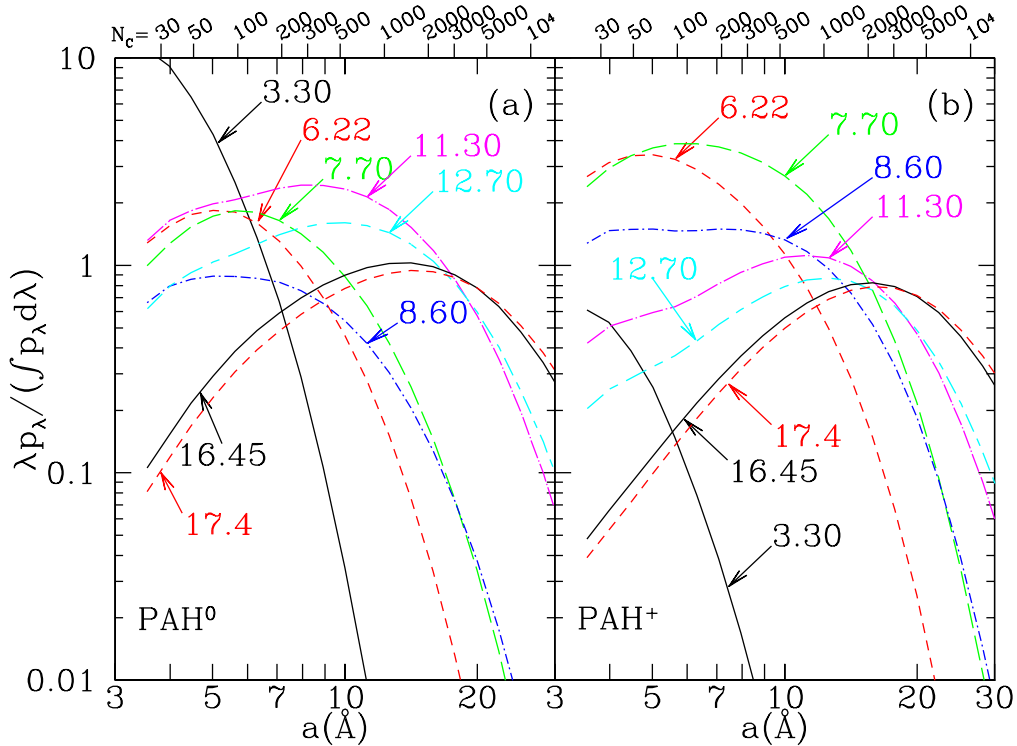


Fig. 6.— Efficiency for radiating in different emission bands, as function of size, for ionized and neutral PAHs (see text).

used to describe small grains that contribute continuum emission into the IRAS $25\mu\text{m}$ band or the MIPS $24\mu\text{m}$ band – here we see that such grains must have effective radii in the $15\text{--}40\text{\AA}$ range to efficiently convert absorbed stellar energy into $\sim 24\mu\text{m}$ continuum emission.

Figures 9 and 10 show $2\text{--}200\mu\text{m}$ emission spectra calculated for carbonaceous grains and amorphous silicate grains with sizes extending from $a = 3.55\text{\AA}$ to 5000\AA . As expected, the emission from $a \gtrsim 60\text{\AA}$ grains peaks at $\lambda \approx 100U^{-1/6}\mu\text{m}$. However, for $U = 10^6$ and 10^7 , λp_λ for $a \gtrsim 60\text{\AA}$ carbonaceous grains has two peaks: one near the peak in λB_λ near $100U^{-1/6}\mu\text{m}$, and the second near $30\mu\text{m}$, the latter resulting from the peak in $C_{\text{abs}}(\lambda)$ near $30\mu\text{m}$ (see Figure 3b). As discussed in §2 above, the $30\mu\text{m}$ opacity peak in the present model produced by graphite in the present model may not apply to the carbonaceous material in interstellar dust.

5. Dust Mixtures

Interstellar dust in the Milky Way and other galaxies includes a wide range of grain sizes. Here we consider the size distributions put forward by WD01 to reproduce the wavelength-dependent extinction on Milky Way sightlines with extinction curves characterized by $R_V \equiv A_V/(A_B - A_V) =$

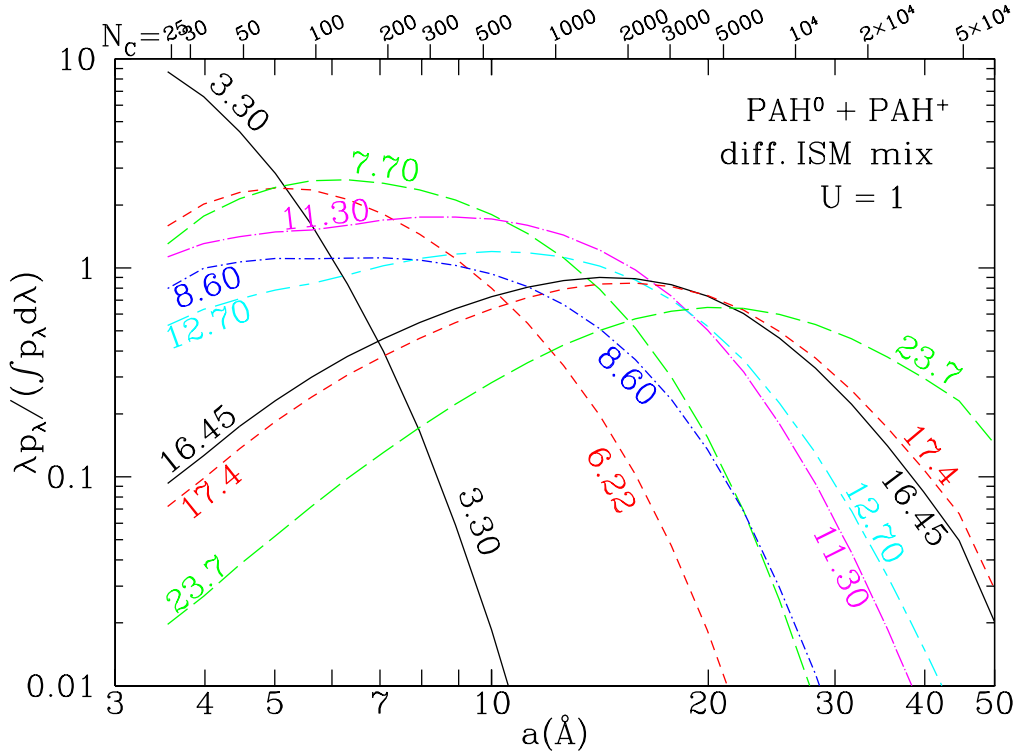


Fig. 7.— λp_λ divided by the the total time-averaged power p radiated by the grain, as a function of grain size a , for selected values of wavelength λ ; curves are labelled by the value of $\lambda(\mu\text{m})$. We assume a mix of neutral and ionized PAHs, with ionization fraction as in Figure 8. $24\mu\text{m}$ is the nominal wavelength of the MIPS band; the other wavelengths are at peaks of emission features.

3.1. WD01 included a population of small ($a \lesssim 50 \text{ \AA}$) carbonaceous particles with specified total mass. Li & Draine (2001a) showed that if these small carbonaceous particles had the physical properties of PAHs and were distributed in two log-normal components,

$$\frac{dn}{da} = \sum_{j=1}^2 \frac{n_{0j}}{a} \exp \left[-\frac{(\ln(a/a_{0j}))^2}{2\sigma_j^2} \right] + \text{non-log-normal contribution} \quad , \quad (11)$$

the resulting infrared emission was approximately consistent with the diffuse emission observed by IRTS (Onaka et al. 1996; Tanaka et al. 1996). The non-log-normal contribution to eq. (11) is given by eq. (4) of WD01. with parameter values taken from that paper except for a reduction in the numbers of grains per H by a factor 0.92, as recommended by Draine (2003). Note that the non-log-normal term also extends continuously down to the smallest sizes.

We continue to use eq. (11) for dn/da , but we have modified the values of the parameters a_{0j} and σ_j , as given in Table 2. The factors n_{0j} in eq. (11) are related to the numbers b_j of carbon

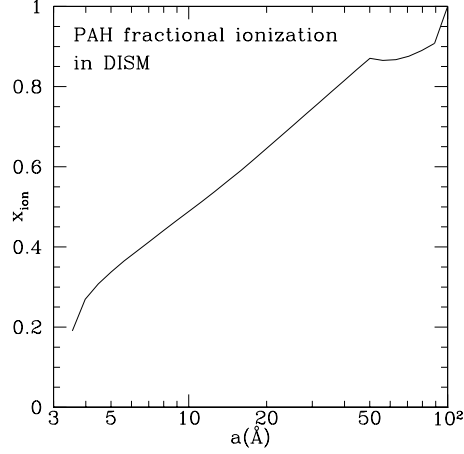


Fig. 8.— Adopted fractional ionization in diffuse ISM (Li & Draine 2001a).

Table 2: PAH Size Distribution Parameters

parameter	LD01	present paper
$b_1/(b_1 + b_2)$	0.75	0.75
$b_2/(b_1 + b_2)$	0.25	0.25
$a_{01}(\text{Å})$	3.5	4.0
$a_{02}(\text{Å})$	30.	20.
σ_1	0.4	0.4
σ_2	0.4	0.55

atoms per total H in each of the log-normal components:

$$n_{0j} = \frac{3}{(2\pi)^{3/2}} \frac{\exp(4.5\sigma_j^2)}{1 + \text{erf}(x_j)} \frac{m_C}{\rho_C a_{Mj}^3 \sigma_j} b_j \quad (12)$$

$$x_j = \frac{\ln(a_{Mj}/a_{\min})}{\sigma_j \sqrt{2}} \quad (13)$$

where ρ_C is the carbon mass density, m_C is the mass of a carbon atom, and

$$a_{Mj} \equiv a_{0j} \exp(3\sigma_j^2) \quad (14)$$

is the location of the peak in the mass distribution $\propto a^3 dn/d \ln a$. Note that the non-log-normal term in eq. (11) also contributes to the population of $N_C < 10^3$ PAHs.

These size distributions have been constructed for various amounts of carbonaceous material in the very small PAH particles. The size distributions all reproduce the observed wavelength-dependent extinction in the Milky Way, for sightlines with $R_V \equiv A_V/E(B-V) \approx 3.1$. Because the abundance of ultrasmall grains is important for the infrared emission as well as other applications, Table 3 gives the amount of carbon present in grains containing $< 10^2$, < 200 , < 500 , $< 10^3$,

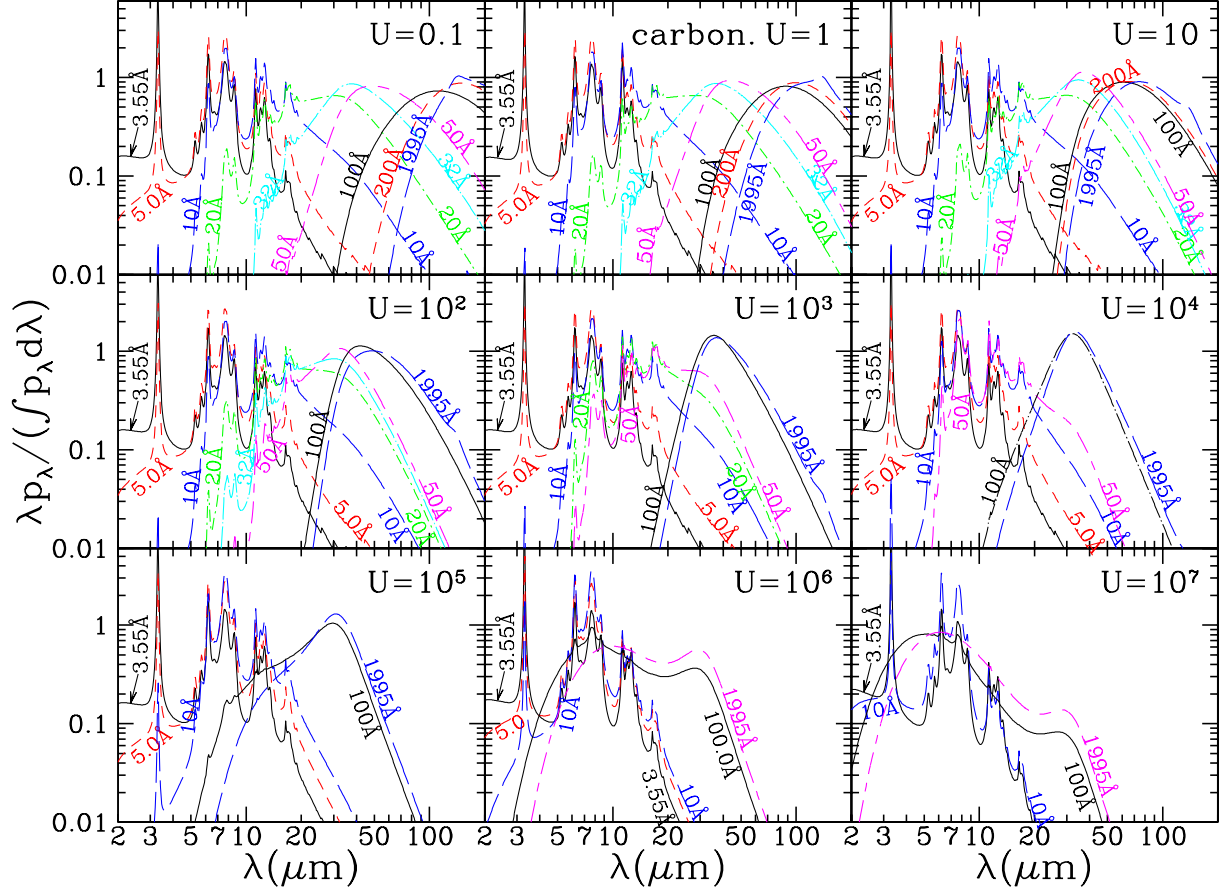


Fig. 9.— Emission for selected sizes of carbonaceous grains for $U = 0.1 - 10^7$. For $a < 100 \text{ \AA}$ PAHs are assumed to have x_{ion} from Fig. 8 (see text).

$< 10^4$, and $< 10^5$ C atoms, for the 7 different grains models. Models $j_M = 1 - 7$ have $(b_1 + b_2) = 0.92 \times 60 \times 10^{-6} \times [(j_M - 1)/6]$. The mass distributions for carbonaceous grains are shown in Fig. 11. [The silicate mass distribution is shown in Fig. 2 of Weingartner & Draine (2001a), except that the dust abundances should be multiplied by 0.92.]

The emissivity per H nucleon for a dust mixture heated by starlight intensity U is

$$j_\nu(U) = \sum_j \int da \frac{dn_j}{da} \int C_{\text{abs}}(j, a, \nu) B_\nu(T) \left(\frac{dP}{dT} \right)_{j,a,U} dT, \quad (15)$$

$$B_\nu(T) \equiv \frac{2h\nu^3}{c^2} \frac{1}{\exp(h\nu/kT) - 1}, \quad (16)$$

where the sum is over compositions j , and the temperature distribution function dP/dT depends on composition j , radius a , and starlight intensity U .

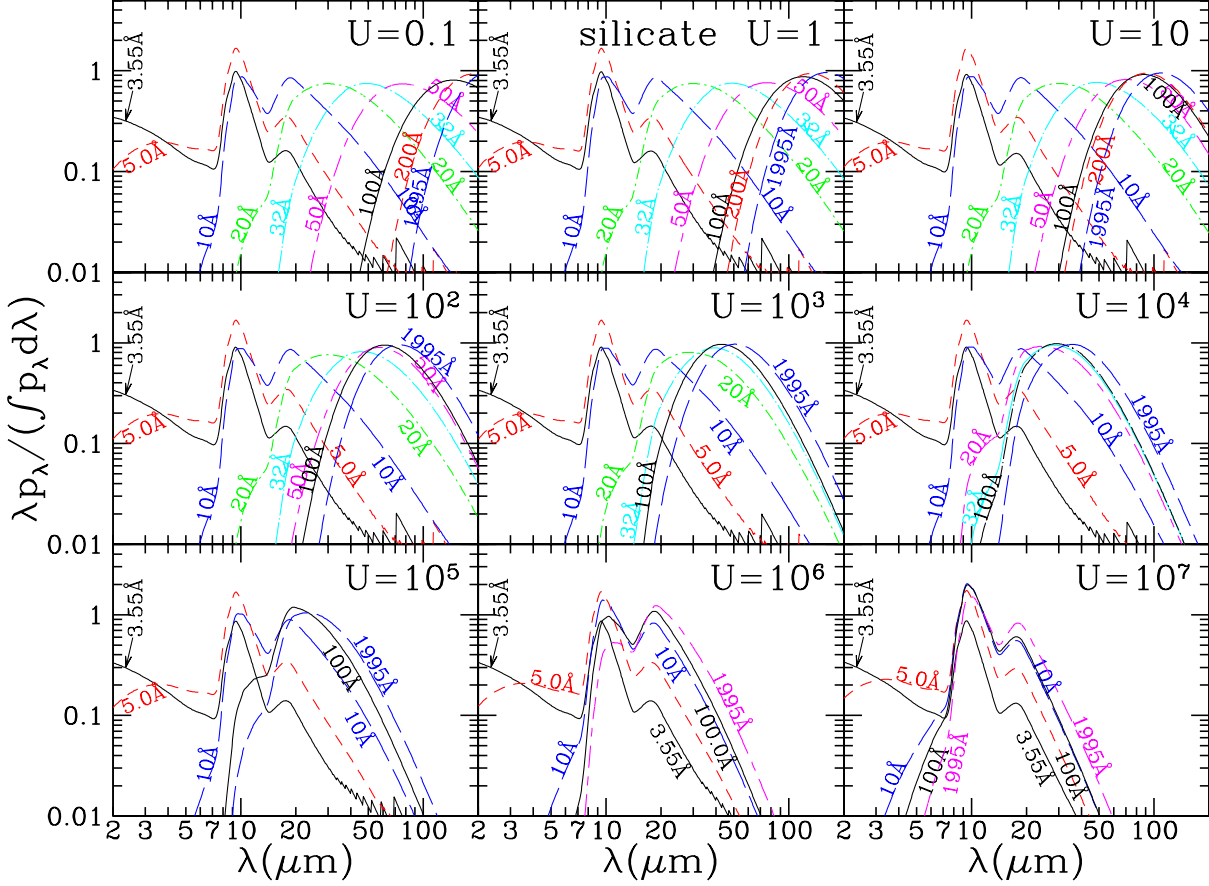


Fig. 10.— Emission for amorphous silicate grains of various sizes for $U = 0.1 - 10^7$ (see text).

Taking dP/dT calculated for the local starlight intensity $U = 1$, summing over the grain size distribution, and over the fractional ionization shown in Fig. 8, we obtain the emission per H nucleon j_λ shown in Figure 12. The emission at $\lambda < 20\mu\text{m}$ depends strongly on the PAH abundance q_{PAH} .

Figure 13 shows the emission calculated for the model with $q_{\text{PAH}} = 4.6\%$, but for different starlight intensities U . For $U \lesssim 10^3$, the normalized emission at $\lambda < 20\mu\text{m}$ is essentially independent of U , because the emission is almost exclusively the result of single-photon heating, with the PAH particles cooling off almost completely between photon absorptions. This remarkable invariance of the PAH emission spectra over orders of magnitude variations in starlight intensities has been observed in a wide range of environments [e.g. see Boulanger et al. (2000), Kahanpää et al. (2003), and Sakon et al. (2004)]. For $U \gtrsim 10^4$, however, the mean time between photon absorptions becomes shorter than the radiative cooling time for a PAH with ~ 1 eV of internal energy, so that the small grains do not cool completely between photon absorptions. Photon absorptions are then able to take them to higher peak temperatures, and the fraction of the power radiated at $\lambda < 20\mu\text{m}$ increases with increasing U .

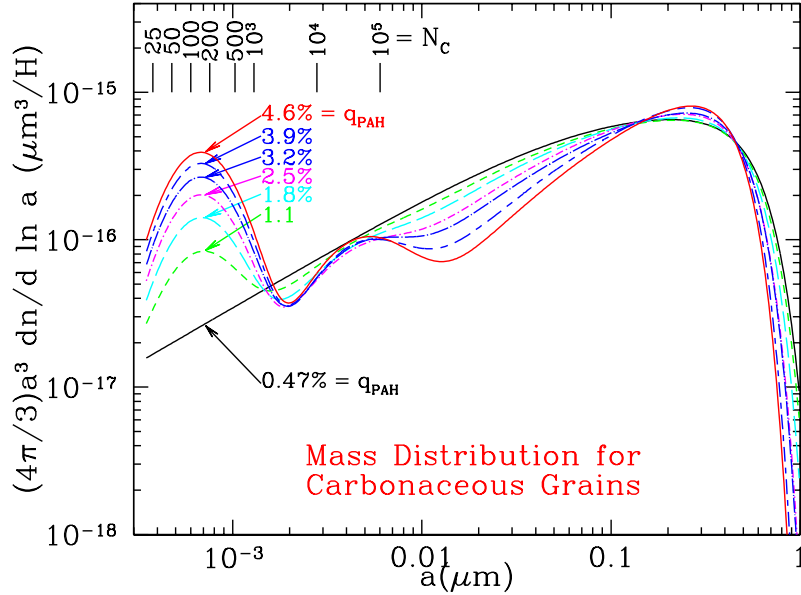


Fig. 11.— Size distributions $j_M=1-7$ for carbonaceous grains. Mass distributions of silicate grains are given by Figure 2 of Weingartner & Draine (2001a), multiplied by 0.92 (see text).

6. Far-IR and Submm Emission

The focus in the present dust model has been on the PAH features, but the model is intended to reproduce the thermal dust emission at far-infrared (FIR) and submm wavelengths as well. The opacities of the amorphous silicate and graphite particles in the model are calculated using the dielectric functions. The graphite dielectric function is based on laboratory measurements of graphite. Because the nature of interstellar amorphous silicate material is uncertain, the far infrared and submm behavior is not constrained by laboratory data. Draine & Lee (1984) made an estimate of the imaginary part of the dielectric function of interstellar amorphous silicate.

Finkbeiner et al. (1999, hereafter FDS) used COBE-FIRAS observations of the sky at high galactic latitudes, after removal of the cosmic background radiation and zodiacal emission, to characterize the emission from diffuse gas and dust in the Milky Way. They excluded $|b| < 7^\circ$, the Magellanic Clouds, HII regions in Orion and Ophiuchus, and an additional 16.3% of the sky where the data were of lower quality. The final data set comprises 81% of the $|b| > 7^\circ$ sky. For this region, FDS find an empirical fit that quite accurately reproduces the observed $100\mu\text{m}-3\text{mm}$ spectra, using two parameters for each pixel: the $100\mu\text{m}$ intensity I_{ν_0} and a temperature T_2 that determines the shape of the $\lambda > 100\mu\text{m}$ spectrum:

$$I_\nu = I_{\nu_0} \frac{(\nu/\nu_0)^{2.70} B_\nu(T_2) + 0.515(\nu/\nu_0)^{1.67} B_\nu(T_1)}{B_{\nu_0}(T_2) + 0.515 B_{\nu_0}(T_1)} \quad ; \quad T_1 = 9.4 \text{ K} \left(\frac{T_2}{16.2 \text{ K}} \right)^{1.182}, \quad (17)$$

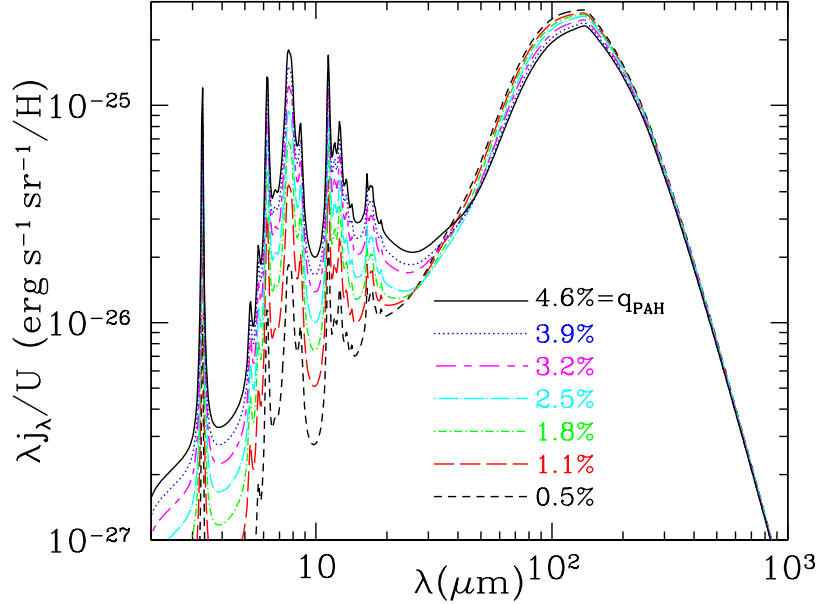


Fig. 12.— Emission spectra for Milky Way dust models with various q_{PAH} (dust models $j_M=1-7$), heated by starlight with $U = 1$. Tabulated spectra for this and other cases will be available at <http://www.astro.princeton.edu/~draine/dust/irem.html>.

where $\nu_0 = c/100\mu\text{m} = 3000$ GHz. The mean value $\langle T_2 \rangle = 16.2$ K. Variations in T_2 are presumably the result of variations in the intensity of the starlight heating the grains; a simple model suggests

$$T_2 = 16.2 \text{ K } U_{\text{FDS}}^{1/6.70}, \quad T_1 = 9.4 \text{ K } U_{\text{FDS}}^{1/5.67}, \quad (18)$$

where U_{FDS} is the intensity of the starlight heating the dust, relative to the average for the region analyzed by FDS.

Based on the observed spectrum of eq. (17) with $T_2 = 16.2$ K, Li & Draine (2001a) made small adjustments to the imaginary part of the dielectric function for the amorphous silicate material at $\lambda > 250\mu\text{m}$ to improved agreement with the observed emission spectrum. The real part of the dielectric function is obtained from the imaginary part using the Kramers-Kronig relations (Draine & Lee 1984). The resulting dielectric function is used to calculate absorption cross sections for amorphous silicate spheres in the present work.

The upper panel of Figure 14a shows the observed far-infrared and submm emission spectrum, as given by eq. (17) with $T_2 = 16.2$ K (i.e., $U_{\text{FDS}} = 1$). Also shown are emission spectra calculated for the present model for two values of the starlight intensity: $U = 0.8$ and $U = 1$. Both spectra have shapes that are close to the observed spectrum, but the $U = 0.8$ spectrum agrees to within a few percent from $100\mu\text{m}$ to 1.5 mm. Evidently $U_{\text{FDS}} \approx 1.2U$ gives the correspondence between the starlight intensity U in the present model (normalized to the estimate of the local interstellar radiation field by Mathis et al. (1983)) and the starlight intensity U_{FDS} relative to the “average”

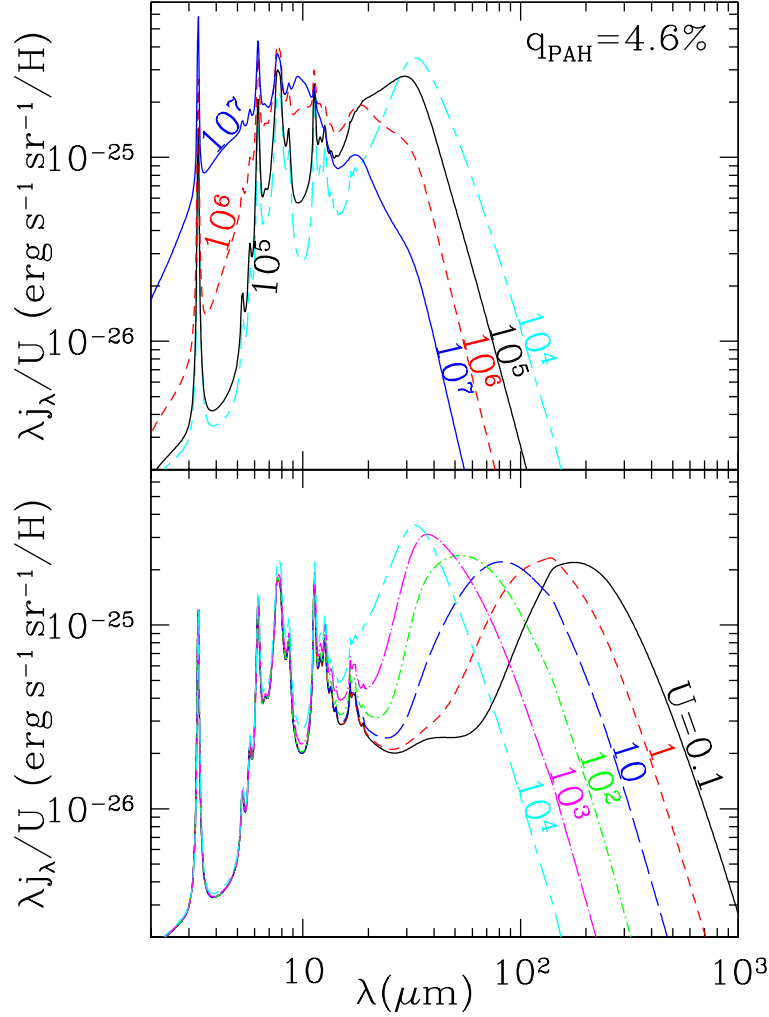


Fig. 13.— Emission spectra for size distribution $j_M = 7$ for selected starlight intensity scale factors U .

for the 71% of the sky analyzed by FDS.

Fig. 14b shows the emission spectra for the model when the radiation field is lowered to $U = 0.5$ and raised to $U = 2$; these spectra compare well with the FDS spectra for $U_{\text{FDS}} = 0.6$ and $U_{\text{FDS}} = 2.4$, as expected from the correspondence $U_{\text{FDS}} \approx 1.2U$ inferred from Fig. 14a.

We conclude that the present dust model can successfully reproduce the emission observed from dust in the diffuse interstellar medium of the Milky Way (including dust in molecular clouds at $|b| > 7$ deg and away from Orion and Ophiuchus) out to wavelengths as long as 2mm without introduction of additional emission components.

Table 3: Physical Dust Models

j_M	Model	$q_{\text{PAH}}(\%)$	$(M_{\text{dust}}/M_{\text{H}})^a$	C/H (ppm) in PAHs with					
				$N_{\text{C}} < 100$	$N_{\text{C}} < 200$	$N_{\text{C}} < 500$	$N_{\text{C}} < 10^3$	$N_{\text{C}} < 10^4$	$N_{\text{C}} < 10^5$
1	MW3.1_00	0.47	0.0100	1.2	1.8	2.9	3.9	8.7	17.0
2	MW3.1_10	1.12	0.0100	3.5	5.6	8.0	9.4	13.6	21.5
3	MW3.1_20	1.77	0.0101	5.8	9.4	13.2	14.9	18.6	26.0
4	MW3.1_30	2.50	0.0102	8.3	13.4	18.6	20.8	24.2	31.1
5	MW3.1_40	3.19	0.0102	10.9	17.6	24.4	27.1	30.7	37.9
6	MW3.1_50	3.90	0.0103	13.5	21.8	30.2	33.4	37.1	44.4
7	MW3.1_60	4.58	0.0104	16.1	26.1	36.1	39.8	43.9	51.6
8	LMC2_00	0.75	0.00343	0.9	1.2	1.8	2.2	3.5	5.0
9	LMC2_05	1.49	0.00344	1.6	2.6	3.7	4.3	5.2	6.7
10	LMC2_10	2.37	0.00359	2.6	4.4	6.3	7.1	7.9	9.6
11	SMC	0.10	0.00206	0.1	0.1	0.2	0.3	0.4	0.5

^a $M_{\text{dust}}/M_{\text{gas}} = (1/1.36)(M_{\text{dust}}/M_{\text{H}})$

7. Spitzer IRAC and MIPS Band Ratios

For interpreting observations with the IRAC and MIPS cameras on Spitzer Space Telescope, the quantities of interest are the band-convolved emissivities and luminosities

$$\langle j_\nu \rangle_{\text{band}} \equiv \frac{\int R_{\text{band}}(\nu) j_\nu d\nu}{\int (\nu/\nu_{\text{band}})^\beta R_{\text{band}}(\nu) d\nu} \quad , \quad \langle L_\nu \rangle_{\text{band}} \equiv \frac{\int R_{\text{band}}(\nu) L_\nu d\nu}{\int (\nu/\nu_{\text{band}})^\beta R_{\text{band}}(\nu) d\nu} \quad (19)$$

and

$$\langle \nu j_\nu \rangle_{\text{band}} \equiv \nu_{\text{band}} \langle j_\nu \rangle_{\text{band}} \quad , \quad \langle \nu L_\nu \rangle_{\text{band}} \equiv \nu_{\text{band}} \langle L_\nu \rangle_{\text{band}} \quad , \quad (20)$$

where $R_{\text{band}}(\nu)$ is the relative response per unit power for the combination of optics, filter, and detector and $\nu_{\text{band}} \equiv c/\lambda_{\text{band}}$, where λ_{band} the nominal wavelength of the band, is given in Table 4.

Table 4 gives $\langle \nu j_\nu \rangle_{\text{band}}$ for the four IRAC bands,⁶ the 2 ‘‘Peakup’’ bands of the Infrared Spectrograph (IRS),⁷ the three MIPS bands,⁸. Table 5 gives emissivities convolved with photometric bands of the AKARI satellite (Kawada et al. 2004; Onaka et al. 2004), and model emissivities convolved with the the three bands of the Herschel PACS instrument,⁹ and the three bands of the

⁶ $R_{\text{band}}(\nu) \propto (1/h\nu)S_{\text{band}}(\nu)$, where the relative response per photon $S_{\text{band}}(\nu)$ is obtained from http://ssc.spitzer.caltech.edu/irac/spectral_response.html. The IRAC calibration uses $\beta = -1$,

⁷ $R_{\text{band}}(\nu) \propto (1/h\nu)S_{\text{band}}(\nu)$, where the relative quantum efficiency $S_{\text{band}}(\nu)$ is given in Fig. 6.1 of the Infrared Spectrograph Data Handbook Version 2.0. The IRS Peakup calibration uses $\beta = -1$.

⁸ $R_{\text{band}}(\nu)$ is obtained from http://ssc.spitzer.caltech.edu/mips/spectral_response.html. The MIPS calibration is for a 10^4 K blackbody, i.e., $\beta = 2$.

⁹ A. Poglitsch has kindly provided provisional $R_{\text{band}}(\nu)$ for PACS. The calibration procedures for PACS have not yet been finalized. Here we assume $\beta = 2$.

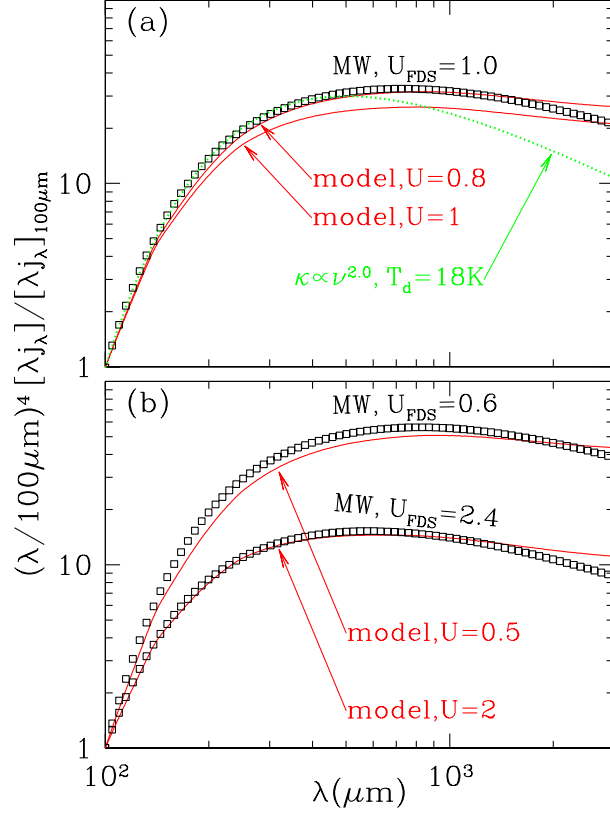


Fig. 14.— (a) Squares: observed spectrum, relative to the $100\mu\text{m}$ emission, of Milky Way dust from Finkbeiner et al. (1999), given by eq. (17,18) with $T_2 = 16.2\text{ K}$. Solid curve: $100\mu\text{m}$ – 3mm emission spectrum for MW dust model with $q_{\text{PAH}} = 4.6\%$, for $U = 0.8$ and 1 . The $U = 0.8$ model approximately reproduces the observed emission for $T_2 = 16.2\text{ K}$, though having excess emission at $\lambda > 1.5\text{ mm}$. The good agreement between the $U = 0.8$ model and the observed spectrum with $U_{\text{FDS}} = 1$ suggests a correspondence $U_{\text{FDS}} \approx 1.2U$. Dotted curve: single-temperature dust model with opacity $\kappa \propto \nu^{2.0}$ and $T = 18\text{ K}$, for comparison. A single modified blackbody produces insufficient emission for $\lambda \gtrsim 500\mu\text{m}$. (b) Observed spectra for $U_{\text{FDS}} = 0.6$ and 2.4 (squares) and the present dust model for $U = 0.5$ and 2 (solid curves).

Herschel SPIRE instrument.¹⁰ are given in Table 6. Emissivities $\langle \nu j_\nu \rangle_{\text{band}}$ are given for selected grain models with several different values of q_{PAH} , and for different values of the starlight intensity scale factor U .

Figure 15 shows $\langle \nu L_\nu \rangle_{\text{band}}$ relative to the total infrared (TIR) dust luminosity

$$L_{\text{TIR}} \equiv \int_0^\infty L_\nu d\nu \quad (21)$$

for 5 bands: IRAC $3.6\mu\text{m}$, IRAC $7.9\mu\text{m}$, MIPS $24\mu\text{m}$, MIPS $71\mu\text{m}$, and MIPS $160\mu\text{m}$. Results are

¹⁰M. Griffin has kindly provided provisional $R_{\text{band}}(\nu)$ for SPIRE. The calibration procedures for SPIRE have not yet been finalized. Here we assume $\beta = 2$.

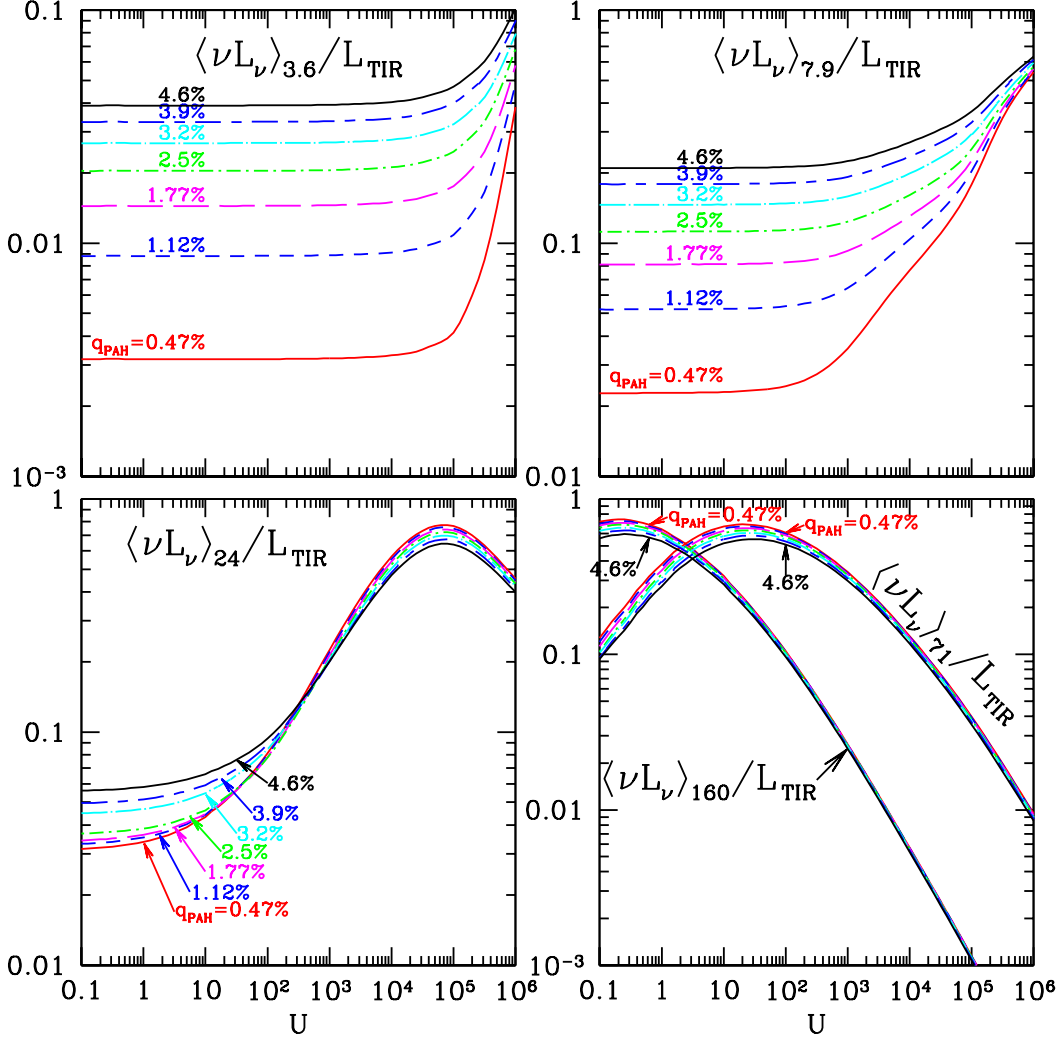


Fig. 15.— IRAC $3.6 \mu\text{m}$, IRAC $7.9 \mu\text{m}$, MIPS $24 \mu\text{m}$, MIPS $71 \mu\text{m}$, and MIPS $160 \mu\text{m}$ band strengths for dust illuminated by a single starlight intensity U , as a function of U , for dust models with 7 different values of q_{PAH} .

given for grain models $j_M = 1-7$, with the model results labelled by the value of q_{PAH} . As expected, the $3.6 \mu\text{m}$ emission and $7.9 \mu\text{m}$ emission per unit total power is entirely the result of single-photon heating at low values of U , and therefore $\langle \nu L_\nu \rangle_{7.9} / L_{\text{TIR}}$ is independent of U for $U \lesssim 10^3$, and $\langle \nu L_\nu \rangle_{3.6} / L_{\text{TIR}}$ is independent of U for $U \lesssim 10^5$. $\langle \nu L_\nu \rangle_{3.6} / L_{\text{TIR}}$ and $\langle \nu L_\nu \rangle_{7.9} / L_{\text{TIR}}$ are also both approximately proportional to q_{PAH} in the low- U limit, as expected. For small values of U , the $24 \mu\text{m}$ emission is also the result of single-photon heating, and $\langle \nu L_\nu \rangle_{24} / L_{\text{TIR}}$ is independent of U for $U \lesssim 10$.

Flagey et al. (2006) extracted the diffuse ISM emission from IRAC imaging of various regions of the Milky Way obtained by the Galactic First Look Survey (GFLS) and the Galactic Legacy

Table 4. Model Emissivities $\langle \nu j_\nu \rangle_{\text{band}}$ (ergs s⁻¹ sr⁻¹/H)^a for Spitzer Space Telescope

U	model q_{PAH} (%)	IRAC 1 3.550 μm	IRAC 2 4.493 μm	IRAC 3 5.731 μm	IRAC 4 7.872 μm	IRS PU1 16 μm	IRS PU2 22. μm	MIPS 1 23.68 μm	MIPS 2 71.42 μm	MIPS 3 155.9 μm
0.5	0.47	5.66e-28	1.54e-28	1.31e-27	4.05e-27	4.86e-27	5.91e-27	5.83e-27	5.04e-26	1.25e-25
0.5	1.12	1.55e-27	4.30e-28	3.53e-27	9.17e-27	6.41e-27	6.27e-27	6.05e-27	4.76e-26	1.21e-25
0.5	1.77	2.56e-27	7.09e-28	5.77e-27	1.43e-26	7.97e-27	6.62e-27	6.26e-27	4.54e-26	1.19e-25
0.5	3.19	4.78e-27	1.34e-27	1.07e-26	2.60e-26	1.24e-26	8.87e-27	8.16e-27	4.11e-26	1.12e-25
0.5	4.58	7.07e-27	1.98e-27	1.58e-26	3.81e-26	1.73e-26	1.14e-26	1.04e-26	3.66e-26	1.05e-25
1.0	0.47	1.13e-27	3.08e-28	2.63e-27	8.10e-27	9.84e-27	1.21e-26	1.20e-26	1.35e-25	2.27e-25
1.0	1.12	3.11e-27	8.59e-28	7.06e-27	1.84e-26	1.29e-26	1.29e-26	1.24e-26	1.28e-25	2.21e-25
1.0	1.77	5.11e-27	1.42e-27	1.15e-26	2.87e-26	1.60e-26	1.35e-26	1.28e-26	1.22e-25	2.18e-25
1.0	3.19	9.55e-27	2.68e-27	2.14e-26	5.20e-26	2.50e-26	1.80e-26	1.66e-26	1.11e-25	2.06e-25
1.0	4.58	1.41e-26	3.96e-27	3.15e-26	7.62e-26	3.47e-26	2.32e-26	2.11e-26	9.89e-26	1.94e-25
3.0	0.47	3.39e-27	9.24e-28	7.90e-27	2.44e-26	3.07e-26	3.95e-26	3.92e-26	5.80e-25	5.19e-25
3.0	1.12	9.32e-27	2.58e-27	2.12e-26	5.51e-26	3.99e-26	4.14e-26	4.03e-26	5.53e-25	5.06e-25
3.0	1.77	1.53e-26	4.25e-27	3.47e-26	8.62e-26	4.91e-26	4.32e-26	4.12e-26	5.35e-25	5.01e-25
3.0	3.19	2.86e-26	8.05e-27	6.41e-26	1.56e-25	7.58e-26	5.66e-26	5.25e-26	4.89e-25	4.77e-25
3.0	4.58	4.24e-26	1.19e-26	9.46e-26	2.29e-25	1.05e-25	7.22e-26	6.60e-26	4.41e-25	4.57e-25
5.0	0.47	5.66e-27	1.54e-27	1.32e-26	4.07e-26	5.28e-26	6.97e-26	6.95e-26	1.08e-24	7.30e-25
5.0	1.12	1.55e-26	4.29e-27	3.53e-26	9.19e-26	6.80e-26	7.27e-26	7.10e-26	1.03e-24	7.13e-25
5.0	1.77	2.56e-26	7.08e-27	5.78e-26	1.44e-25	8.32e-26	7.54e-26	7.23e-26	1.00e-24	7.06e-25
5.0	3.19	4.77e-26	1.34e-26	1.07e-25	2.60e-25	1.28e-25	9.76e-26	9.10e-26	9.20e-25	6.76e-25
5.0	4.58	7.06e-26	1.98e-26	1.58e-25	3.81e-25	1.77e-25	1.24e-25	1.14e-25	8.36e-25	6.50e-25
10.0	0.47	1.13e-26	3.08e-27	2.63e-26	8.17e-26	1.12e-25	1.54e-25	1.54e-25	2.37e-24	1.13e-24
10.0	1.12	3.11e-26	8.59e-27	7.07e-26	1.84e-25	1.42e-25	1.59e-25	1.56e-25	2.27e-24	1.11e-24
10.0	1.77	5.11e-26	1.42e-26	1.15e-25	2.88e-25	1.72e-25	1.63e-25	1.57e-25	2.21e-24	1.10e-24
10.0	3.19	9.55e-26	2.68e-26	2.14e-25	5.21e-25	2.61e-25	2.07e-25	1.94e-25	2.05e-24	1.06e-24
10.0	4.58	1.41e-25	3.96e-26	3.15e-25	7.63e-25	3.59e-25	2.59e-25	2.39e-25	1.88e-24	1.02e-24
100.0	0.47	1.13e-25	3.09e-26	2.67e-25	8.67e-25	1.68e-24	2.80e-24	2.89e-24	2.16e-23	3.72e-24
100.0	1.12	3.11e-25	8.62e-26	7.12e-25	1.89e-24	1.94e-24	2.78e-24	2.83e-24	2.09e-23	3.66e-24
100.0	1.77	5.12e-25	1.42e-25	1.16e-24	2.93e-24	2.20e-24	2.75e-24	2.77e-24	2.06e-23	3.64e-24
100.0	3.19	9.57e-25	2.69e-25	2.15e-24	5.26e-24	3.07e-24	3.09e-24	3.03e-24	1.95e-23	3.55e-24
100.0	4.58	1.41e-24	3.97e-25	3.17e-24	7.70e-24	4.07e-24	3.56e-24	3.41e-24	1.85e-23	3.48e-24

^a Additional models, with spectra, are available online at <http://www.astro.princeton.edu/~draine/dust/irem.html>

Table 5. Model Emissivities $\langle \nu j_\nu \rangle_{\text{band}}$ (ergs s⁻¹ sr⁻¹/H)^a for Akari

U	model q_{PAH} (%)	N3 3.2 μm	N4 4.1 μm	S7 7.0 μm	S9W 9.0 μm	S11 11.0 μm	L15 15. μm	L18W 18. μm	L24 24. μm	N60 65. μm	WIDE-S 80. μm	WIDE-L 140. μm	N160 160. μm
0.5	0.47	3.75e-28	1.68e-28	4.37e-27	3.55e-27	3.49e-27	5.13e-27	5.48e-27	5.88e-27	4.46e-26	8.43e-26	1.32e-25	1.26e-25
0.5	1.12	1.03e-27	4.67e-28	1.03e-26	7.54e-27	6.36e-27	6.71e-27	6.38e-27	6.18e-27	4.20e-26	8.02e-26	1.28e-25	1.22e-25
0.5	1.77	1.69e-27	7.70e-28	1.62e-26	1.16e-26	9.26e-27	8.30e-27	7.28e-27	6.47e-27	3.99e-26	7.73e-26	1.25e-25	1.20e-25
0.5	3.19	3.16e-27	1.46e-27	2.95e-26	2.09e-26	1.63e-26	1.29e-26	1.06e-26	8.57e-27	3.62e-26	7.04e-26	1.18e-25	1.13e-25
0.5	4.58	4.68e-27	2.15e-27	4.33e-26	3.05e-26	2.36e-26	1.79e-26	1.42e-26	1.10e-26	3.25e-26	6.31e-26	1.10e-25	1.06e-25
1.0	0.47	7.50e-28	3.35e-28	8.75e-27	7.12e-27	7.01e-27	1.04e-26	1.12e-26	1.21e-26	1.23e-25	2.03e-25	2.48e-25	2.25e-25
1.0	1.12	2.05e-27	9.33e-28	2.06e-26	1.51e-26	1.27e-26	1.35e-26	1.30e-26	1.27e-26	1.16e-25	1.93e-25	2.40e-25	2.19e-25
1.0	1.77	3.37e-27	1.54e-27	3.25e-26	2.31e-26	1.85e-26	1.67e-26	1.47e-26	1.32e-26	1.11e-25	1.87e-25	2.36e-25	2.16e-25
1.0	3.19	6.32e-27	2.91e-27	5.90e-26	4.18e-26	3.26e-26	2.59e-26	2.13e-26	1.74e-26	1.01e-25	1.71e-25	2.22e-25	2.04e-25
1.0	4.58	9.34e-27	4.30e-27	8.66e-26	6.10e-26	4.72e-26	3.60e-26	2.86e-26	2.23e-26	8.97e-26	1.55e-25	2.09e-25	1.93e-25
3.0	0.47	2.25e-27	1.01e-27	2.63e-26	2.14e-26	2.12e-26	3.24e-26	3.56e-26	3.93e-26	5.66e-25	7.27e-25	5.93e-25	5.01e-25
3.0	1.12	6.16e-27	2.80e-27	6.17e-26	4.54e-26	3.84e-26	4.18e-26	4.08e-26	4.08e-26	5.38e-25	6.98e-25	5.78e-25	4.89e-25
3.0	1.77	1.01e-26	4.62e-27	9.76e-26	6.95e-26	5.58e-26	5.12e-26	4.60e-26	4.23e-26	5.19e-25	6.80e-25	5.71e-25	4.84e-25
3.0	3.19	1.89e-26	8.73e-27	1.77e-25	1.25e-25	9.80e-26	7.88e-26	6.56e-26	5.48e-26	4.73e-25	6.28e-25	5.43e-25	4.61e-25
3.0	4.58	2.80e-26	1.29e-26	2.60e-25	1.83e-25	1.42e-25	1.09e-25	8.77e-26	6.95e-26	4.24e-25	5.76e-25	5.17e-25	4.42e-25
5.0	0.47	3.75e-27	1.68e-27	4.39e-26	3.59e-26	3.57e-26	5.58e-26	6.20e-26	6.93e-26	1.09e-24	1.25e-24	8.52e-25	6.96e-25
5.0	1.12	1.03e-26	4.67e-27	1.03e-25	7.57e-26	6.43e-26	7.12e-26	7.05e-26	7.16e-26	1.04e-24	1.20e-24	8.32e-25	6.80e-25
5.0	1.77	1.69e-26	7.70e-27	1.63e-25	1.16e-25	9.33e-26	8.68e-26	7.90e-26	7.37e-26	1.00e-24	1.17e-24	8.23e-25	6.74e-25
5.0	3.19	3.16e-26	1.45e-26	2.95e-25	2.09e-25	1.64e-25	1.33e-25	1.12e-25	9.45e-26	9.18e-25	1.09e-24	7.85e-25	6.45e-25
5.0	4.58	4.67e-26	2.15e-26	4.33e-25	3.05e-25	2.37e-25	1.83e-25	1.48e-25	1.19e-25	8.29e-25	1.01e-24	7.53e-25	6.22e-25
10.0	0.47	7.50e-27	3.35e-27	8.82e-26	7.22e-26	7.25e-26	1.18e-25	1.34e-25	1.52e-25	2.48e-24	2.50e-24	1.36e-24	1.06e-24
10.0	1.12	2.05e-26	9.33e-27	2.06e-25	1.52e-25	1.30e-25	1.48e-25	1.50e-25	1.55e-25	2.37e-24	2.41e-24	1.33e-24	1.04e-24
10.0	1.77	3.37e-26	1.54e-26	3.25e-25	2.32e-25	1.87e-25	1.79e-25	1.66e-25	1.59e-25	2.30e-24	2.36e-24	1.32e-24	1.04e-24
10.0	3.19	6.32e-26	2.91e-26	5.90e-25	4.18e-25	3.28e-25	2.71e-25	2.31e-25	2.00e-25	2.12e-24	2.21e-24	1.26e-24	9.96e-25
10.0	4.58	9.34e-26	4.30e-26	8.67e-25	6.11e-25	4.74e-25	3.72e-25	3.05e-25	2.50e-25	1.93e-24	2.06e-24	1.22e-24	9.65e-25
100.0	0.47	7.51e-26	3.37e-26	9.26e-25	7.97e-25	8.76e-25	1.72e-24	2.11e-24	2.63e-24	2.55e-23	1.77e-23	4.84e-24	3.36e-24
100.0	1.12	2.05e-25	9.37e-26	2.11e-24	1.59e-24	1.44e-24	1.99e-24	2.22e-24	2.60e-24	2.47e-23	1.72e-23	4.75e-24	3.30e-24
100.0	1.77	3.38e-25	1.54e-25	3.30e-24	2.39e-24	2.00e-24	2.25e-24	2.33e-24	2.57e-24	2.43e-23	1.70e-23	4.73e-24	3.29e-24
100.0	3.19	6.33e-25	2.92e-25	5.96e-24	4.26e-24	3.41e-24	3.16e-24	2.95e-24	2.91e-24	2.29e-23	1.62e-23	4.60e-24	3.20e-24
100.0	4.58	9.36e-25	4.31e-25	8.74e-24	6.19e-24	4.88e-24	4.20e-24	3.69e-24	3.36e-24	2.15e-23	1.55e-23	4.51e-24	3.15e-24

^a Additional models, with spectra, are available online at <http://www.astro.princeton.edu/~draine/dust/irem.html>

Table 6. Model Emissivities $\langle \nu j_\nu \rangle_{\text{band}}$ (ergs s⁻¹ sr⁻¹/H)^a for Herschel

U	model q_{PAH} (%)	PACS 1 75 μm	PACS 2 110 μm	PACS 3 170 μm	SPIRE 1 250 μm	SPIRE 2 360 μm	SPIRE 3 520 μm
0.5	0.47	4.21e-26	7.92e-26	9.61e-26	5.71e-26	2.05e-26	5.80e-27
0.5	1.12	3.97e-26	7.57e-26	9.31e-26	5.58e-26	2.01e-26	5.70e-27
0.5	1.77	3.78e-26	7.34e-26	9.17e-26	5.53e-26	2.00e-26	5.68e-27
0.5	3.19	3.43e-26	6.71e-26	8.61e-26	5.28e-26	1.92e-26	5.50e-27
0.5	4.58	3.05e-26	6.05e-26	8.09e-26	5.07e-26	1.87e-26	5.39e-27
1.0	0.47	1.13e-25	1.78e-25	1.73e-25	8.74e-26	2.83e-26	7.50e-27
1.0	1.12	1.08e-25	1.71e-25	1.68e-25	8.55e-26	2.77e-26	7.38e-27
1.0	1.77	1.03e-25	1.67e-25	1.66e-25	8.48e-26	2.76e-26	7.35e-27
1.0	3.19	9.33e-26	1.53e-25	1.57e-25	8.13e-26	2.66e-26	7.13e-27
1.0	4.58	8.32e-26	1.40e-25	1.48e-25	7.85e-26	2.60e-26	7.01e-27
3.0	0.47	4.96e-25	5.69e-25	3.94e-25	1.56e-25	4.40e-26	1.07e-26
3.0	1.12	4.73e-25	5.49e-25	3.84e-25	1.53e-25	4.32e-26	1.05e-26
3.0	1.77	4.57e-25	5.37e-25	3.80e-25	1.52e-25	4.30e-26	1.05e-26
3.0	3.19	4.17e-25	5.00e-25	3.62e-25	1.47e-25	4.17e-26	1.02e-26
3.0	4.58	3.76e-25	4.64e-25	3.47e-25	1.43e-25	4.09e-26	1.01e-26
5.0	0.47	9.28e-25	9.23e-25	5.54e-25	1.99e-25	5.29e-26	1.25e-26
5.0	1.12	8.87e-25	8.92e-25	5.41e-25	1.95e-25	5.20e-26	1.23e-26
5.0	1.77	8.59e-25	8.75e-25	5.36e-25	1.94e-25	5.18e-26	1.22e-26
5.0	3.19	7.89e-25	8.20e-25	5.12e-25	1.88e-25	5.03e-26	1.19e-26
5.0	4.58	7.17e-25	7.67e-25	4.93e-25	1.83e-25	4.94e-26	1.18e-26
10.0	0.47	2.04e-24	1.71e-24	8.59e-25	2.73e-25	6.77e-26	1.53e-26
10.0	1.12	1.96e-24	1.66e-24	8.41e-25	2.68e-25	6.67e-26	1.51e-26
10.0	1.77	1.91e-24	1.63e-24	8.35e-25	2.67e-25	6.64e-26	1.50e-26
10.0	3.19	1.76e-24	1.54e-24	8.02e-25	2.59e-25	6.47e-26	1.47e-26
10.0	4.58	1.62e-24	1.45e-24	7.77e-25	2.54e-25	6.36e-26	1.45e-26
100.0	0.47	1.88e-23	9.29e-24	2.84e-24	6.49e-25	1.35e-25	2.75e-26
100.0	1.12	1.82e-23	9.08e-24	2.79e-24	6.40e-25	1.33e-25	2.71e-26
100.0	1.77	1.79e-23	9.00e-24	2.78e-24	6.38e-25	1.33e-25	2.71e-26
100.0	3.19	1.70e-23	8.66e-24	2.71e-24	6.24e-25	1.30e-25	2.66e-26
100.0	4.58	1.61e-23	8.39e-24	2.66e-24	6.17e-25	1.29e-25	2.64e-26

^a Additional models, with spectra, are available online at <http://www.astro.princeton.edu/~draine/dust/irem.html>

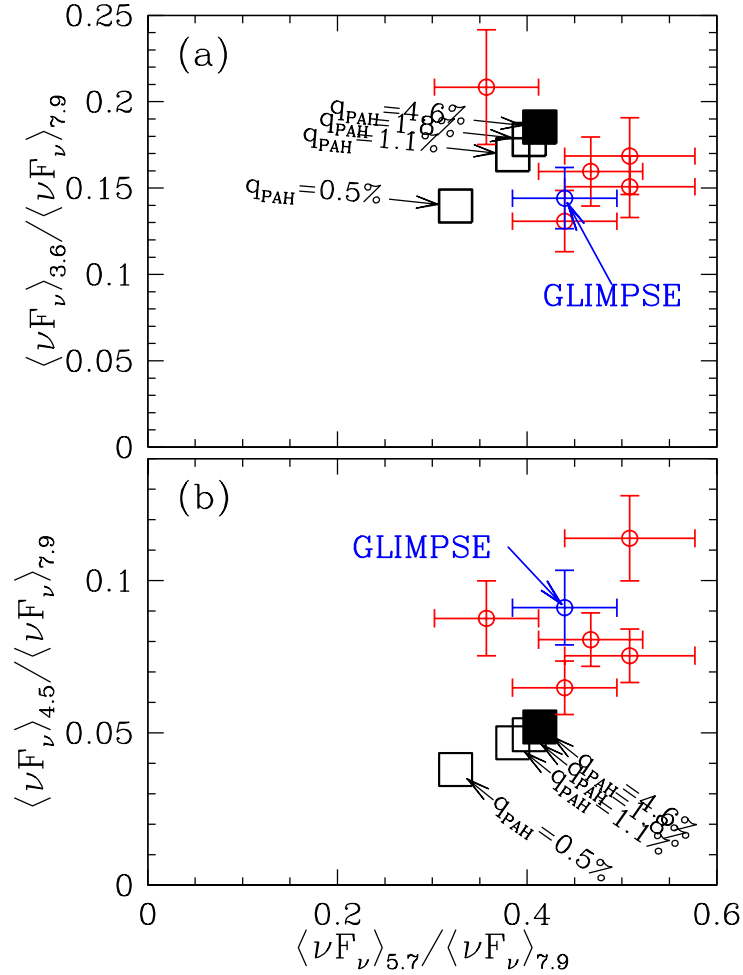


Fig. 16.— IRAC color-color plots for dust emission. Symbols with error bars: diffuse emission extracted by Flagey et al. (2006) for 5 GFLS fields and for one GLIMPSE field. Squares: present models for Milky Way dust with different values of $q_{\text{PAH}} = 0.47\%$, 1.1% , 1.8% , and 4.6% , for starlight intensities $U \lesssim 10^3$ so that single-photon heating is dominant. The dust model appears consistent with the observed diffuse emission in IRAC 3.6, 5.7, and $7.9\mu\text{m}$ bands, but observed emission in the $4.5\mu\text{m}$ band appears to be about 50% stronger than given by the model emissivities.

Infrared MidPlane Survey Extraordinaire (GLIMPSE). The model emission spectra, convolved with the response function for the IRAC bands, can be compared to the observed colors of the diffuse emission.

Figure 16a shows the colors of the observed emission in the IRAC $3.6\mu\text{m}$, $5.7\mu\text{m}$, and $7.9\mu\text{m}$ bands. The filled squares show the color calculated for the present dust model with the value of $q_{\text{PAH}} \approx 4.6\%$ that appears to be applicable to the dust in the Milky Way and other spiral galaxies with near-solar metallicity (Draine et al. 2006). The model with $q_{\text{PAH}} \approx 4.6\%$ appears to be in

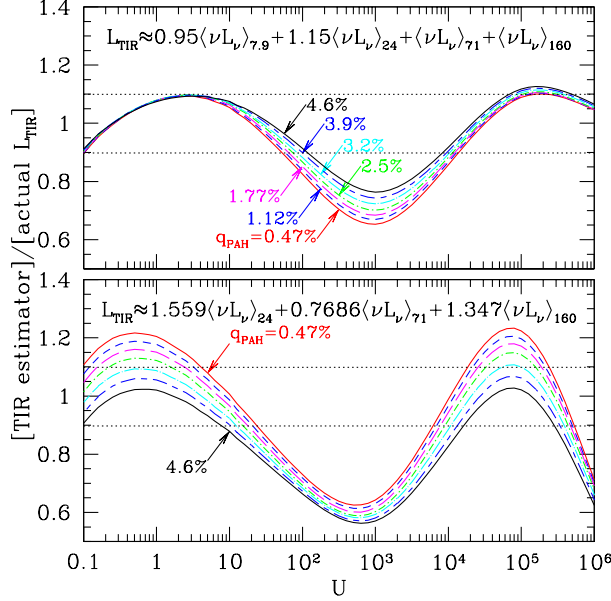


Fig. 17.— Upper panel: estimator (22) for total infrared flux (TIR) divided by actual TIR. The estimator (22) is within $\pm 10\%$ of the actual TIR (within the dotted lines) for $0.1 < U \lesssim 10^2$ and $10^4 \lesssim U < 10^6$. Lower panel: the TIR estimator from Dale & Helou (2002), applied to the present dust models.

good agreement with the Milky Way observations in Figure 16a. First of all, $\langle \nu F_\nu \rangle_{5.7} / \langle \nu F_\nu \rangle_{7.9}$ is within the range of observed values, indicating that the adopted $C_{\text{abs}}(\lambda)$ has approximately the correct shape over the $5.5\text{--}8.5\ \mu\text{m}$ wavelength range. Second, the ratio of $3.6\ \mu\text{m}$ emission divided by $8.0\ \mu\text{m}$ emission is close to the observed value. The emission into the IRAC $3.6\ \mu\text{m}$ band is sensitive to the abundances of the very smallest PAHs, with $N_C \lesssim 75$ (see Figure 6), we can therefore conclude that the size distribution adopted by the present model has approximately the correct amount of PAH mass in the interval $25 \lesssim N_C \lesssim 75$, at least relative to the PAH mass in the interval $25 \lesssim N_C \lesssim 10^3$ that radiates efficiently into the IRAC $8\ \mu\text{m}$ band. The ratio of the $3.6\ \mu\text{m}$ emission to the $8\ \mu\text{m}$ emission of course is sensitive to the assumed PAH charge state (see Fig. 6). The present model assumes a mixture of ionization conditions that is intended to be representative of the local interstellar medium (see Figure 8). If the actual ionized fraction for the PAHs is higher than in our model, then the actual mass fraction in the $25 \lesssim N_C \lesssim 75$ would have to be even higher than the adopted size distribution (shown in Figure 11). Conversely, if the PAH neutral fraction is actually higher than in our model, then the PAH mass fraction in the $25 \lesssim N_C \lesssim 75$ range could be reduced.

Observations of external galaxies by ISO and Spitzer Space Telescope have been interpreted as showing diffuse nonstellar emission in the $2.5\text{--}5\ \mu\text{m}$ wavelength range (Lu et al. 2003; Helou et al. 2004), consistent with thermal emission from dust with $Q_{\text{abs}} \propto \nu^2$ and temperatures in the $\sim 750\text{--}1000\ \text{K}$ range. The GFLS and GLIMPSE images also appear to contain diffuse emission in the

4.5 μm band (Flagey et al. 2006). Figure 16b shows the observed ratio of 4.5 μm emission relative to 7.9 μm emission as well as the model values. The observed 4.5 μm emission is perhaps 50% stronger (relative to the 8.0 μm emission) than the models.

In many cases it is desirable to try to estimate the total infrared luminosity from the observed fluxes in the IRAC and MIPS bands. The following weighted sum of IRAC 7.9 μm and the 3 MIPS bands is a reasonably accurate estimator for L_{TIR} :

$$L_{\text{TIR}} \approx 0.95 \langle \nu L_\nu \rangle_{7.9} + 1.15 \langle \nu L_\nu \rangle_{24} + \langle \nu L_\nu \rangle_{71} + \langle \nu L_\nu \rangle_{160} \quad . \quad (22)$$

Figure 17 plots this estimator relative to the actual L_{TIR} for our dust models, showing that eq. (22) allows the total infrared luminosity to be estimated to within $\sim 10\%$ for our dust models heated by starlight with $0.1 \lesssim U \lesssim 10^2$ or with $10^4 \lesssim U \lesssim 10^6$. The accuracy becomes somewhat lower for $10^2 \lesssim U \lesssim 10^4$ (because of the factor of 3 gap in wavelength between the 71 μm band and the 24 μm band), but the worst-case error is only $\sim 30\%$, occurring for $U \approx 10^3$ where the FIR emission peak falls at $\sim 40 \mu\text{m}$, halfway between the MIPS 24 μm and 71 μm filters, with the result that MIPS photometry underestimates the actual power. Also plotted in Figure 17 is the TIR estimator proposed by Dale & Helou (2002) using only MIPS photometry, applied to our models. The Dale & Helou (2002) luminosity estimate is accurate to within $\pm 25\%$ for $U \lesssim 10^2$.

8. Emission Spectra for Dust Models: Distribution of Starlight Intensities

The dust grains in a galaxy will be exposed to a wide range of starlight intensities. The bulk of the dust in the diffuse interstellar medium will be heated by a general diffuse radiation field contributed by many stars. However, some dust grains will happen to be located in regions close to luminous stars, such as photodissociation regions near OB stars, where the starlight heating the dust will be much more intense than the diffuse starlight illuminating the bulk of the grains.

In principle, one could construct a model for the distribution of stars and dust in the galaxy, and solve the radiative transfer problem to determine the heating rate for each dust grain. This, however, requires many uncertain assumptions, as well as heavy numerical calculations to solve the radiative transfer problem [see, e.g., Witt & Gordon (1996); Silva et al. (1998); Popescu et al. (2000); Tuffs et al. (2004); Piovan et al. (2006)]. Here we take a much simpler approach, and assume a simple parametric form for the fraction of the dust mass exposed to a distribution of starlight intensities U described by a delta function and a power-law distribution for $U_{\text{min}} < U < U_{\text{max}}$:

$$\frac{dM_{\text{dust}}}{dU} = (1 - \gamma) M_{\text{dust}} \delta(U - U_{\text{min}}) + \gamma M_{\text{dust}} \frac{(\alpha - 1)}{[U_{\text{min}}^{1-\alpha} - U_{\text{max}}^{1-\alpha}]} U^{-\alpha} \quad , \quad \alpha \neq 1, \quad (23)$$

where dM_{dust} is the mass of dust heated by starlight intensities in $[U, U + dU]$; M_{dust} is the total mass of dust, $(1 - \gamma)$ is the fraction of the dust mass that is exposed to starlight intensity U_{min} , and α is a power-law index. This functional form is similar to the power-law distribution used by Dale et al. (2001) and Dale & Helou (2002), except that we have added a delta function component

that contains most of the dust mass; the delta-function term is intended to represent the dust in the general diffuse interstellar medium.

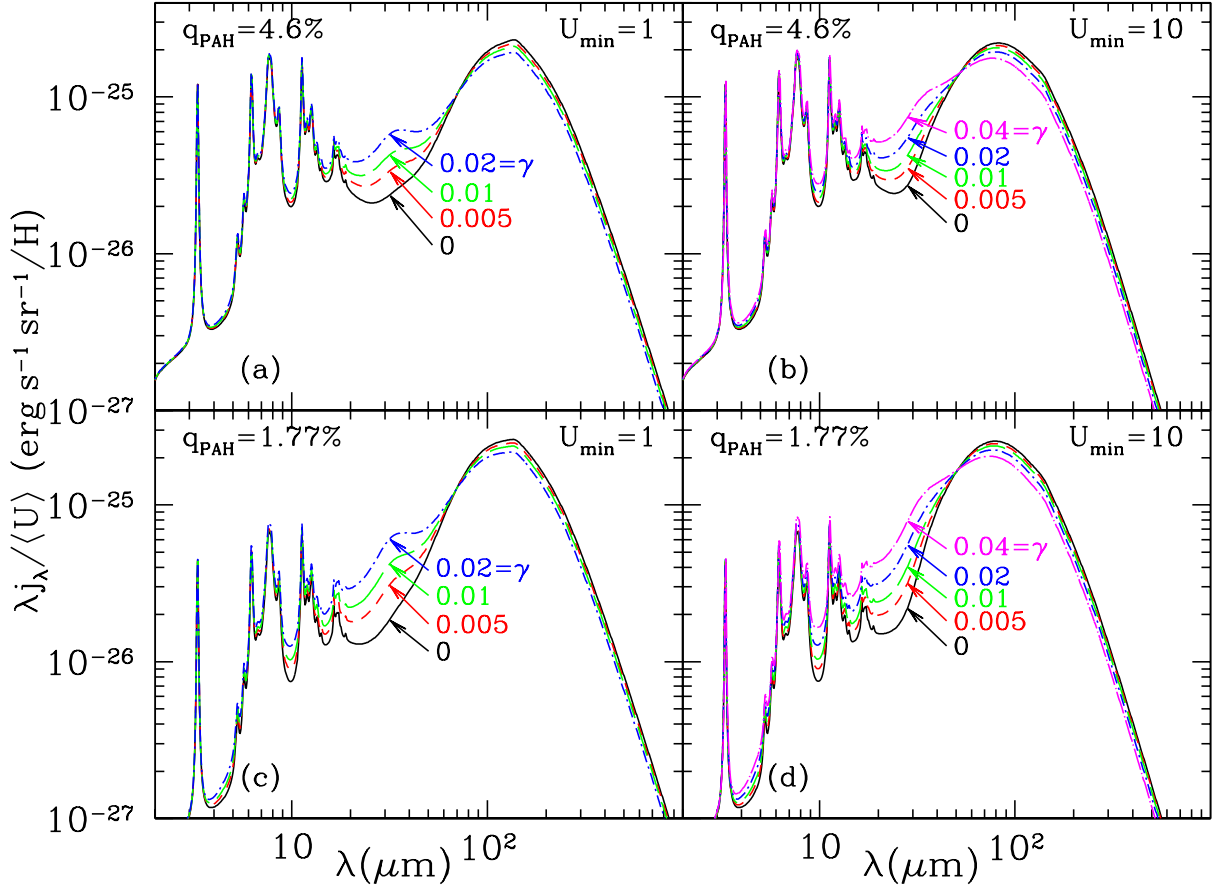


Fig. 18.— Emission spectra for models with MW dust with (a) $q_{\text{PAH}} = 4.6\%$, $U_{\text{min}} = 1$, (b) $q_{\text{PAH}} = 4.6\%$, $U_{\text{min}} = 10$, (c) $q_{\text{PAH}} = 1.77\%$, $U_{\text{min}} = 1$, (d) $q_{\text{PAH}} = 1.77\%$, $U_{\text{min}} = 10$. All models with $U_{\text{max}} = 10^6$, $\alpha = 2$. Values of γ are indicated.

The starlight distribution function eq. (23) has parameters U_{min} , U_{max} , α , and γ . However, Draine et al. (2006) find that the SEDs of galaxies in the SINGS survey appear to be satisfactorily reproduced with fixed $\alpha = 2$ and $U_{\text{max}} = 10^6$, and we will therefore use these fixed values for α and U_{max} . For $\alpha = 2$ the fraction γ of the dust mass that is exposed to starlight intensities $U_{\text{min}} < U \leq U_{\text{max}}$ has equal amounts of infrared power per unit $\log U$. Each of the grain models in Table 3 has a different value of q_{PAH} , so the parameter q_{PAH} serves as a proxy for the dust model. This leaves us with four free parameters: M_{dust} , q_{PAH} , U_{min} , γ . The shape of the dust emission spectrum is determined by only 3 free parameters: q_{PAH} , U_{min} , and γ . Examples of emission spectra are shown in Figure 18.

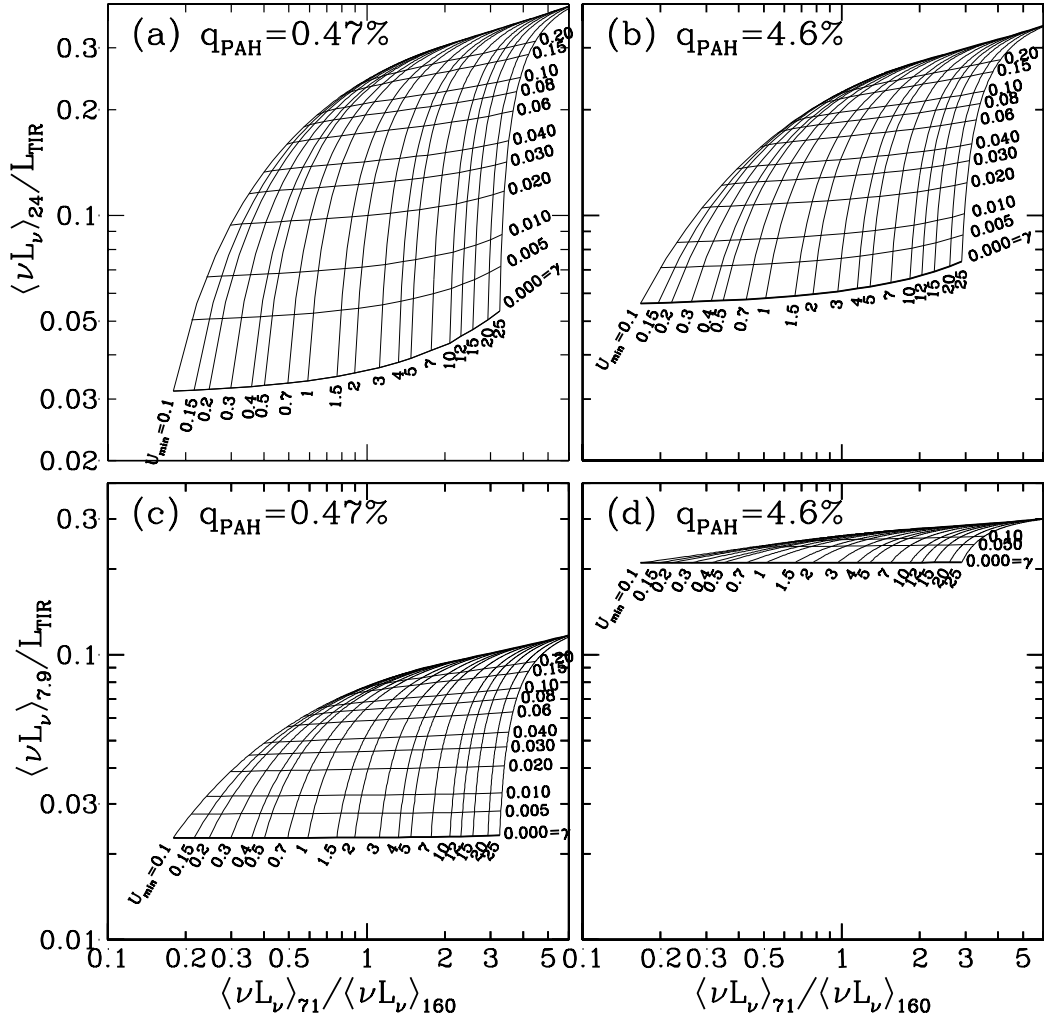


Fig. 19.— Ratios of $\langle \nu L_\nu \rangle_{7.9} / L_{\text{TIR}}$ and $\langle \nu L_\nu \rangle_{24} / L_{\text{TIR}}$ for dust models with $q_{\text{PAH}} = 0.47\%$ and 4.6% , plotted against the ratio $\langle \nu L_\nu \rangle_{71} / \langle \nu L_\nu \rangle_{160}$. The model grids are labelled by the minimum starlight intensity U_{min} and the fraction γ of the dust exposed to starlight with $U > U_{\text{min}}$ (see text).

9. Estimating q_{PAH} , U_{min} , γ , f_{PDR} , and M_{dust}

Photometry obtained with the IRAC and MIPS cameras on Spitzer Space Telescope can be used to estimate the free parameters q_{PAH} , U_{min} , and γ , the fraction f_{PDR} of the dust infrared emission radiated by dust grains in photodissociation regions where $U > 10^2$, and the total dust mass M_{dust} . The flux measured in the IRAC $3.6\mu\text{m}$ band is almost entirely due to starlight, and therefore can be used to remove the starlight contribution to the $7.9\mu\text{m}$ and $24\mu\text{m}$ bands, with the

nonstellar flux densities estimated to be

$$F_{\nu}^{\text{ns}}(7.9\mu\text{m}) = F_{\nu}(7.9\mu\text{m}) - 0.232F_{\nu}(3.6\mu\text{m}) \quad (24)$$

$$F_{\nu}^{\text{ns}}(24\mu\text{m}) = F_{\nu}(24\mu\text{m}) - 0.032F_{\nu}(3.6\mu\text{m}) \quad (25)$$

where the coefficients 0.232 and 0.032 are from Helou et al. (2004). The stellar contribution to the 71 μm and 160 μm bands is negligible.

For a given dust type (i.e., a given value of q_{PAH}) there is a two dimensional family of emission models, parameterized by U_{min} and γ . Figures 19a and b show the flux into the MIPS 24 μm band normalized by the total dust luminosity L_{TIR} , plotted against the ratio of the fluxes into the MIPS 71 μm and 160 μm bands. The two-dimensional family of emission models is shown, for $0.1 \leq U_{\text{min}} \leq 20$, and $0 \leq \gamma \leq 0.20$. The models with $\gamma = 0$ (the lower boundary of the model grid) are models with dust heated by a single starlight intensity: $\langle U \rangle = U_{\text{min}}$.

For the $\gamma = 0$ models, the ratio $(\nu L_{\nu})_{24}/L_{\text{TIR}}$ is essentially independent of U_{min} for $U_{\text{min}} \lesssim 2$, as already seen in Figure 15: the emission into the 24 μm band is dominated by single-photon heating of small grains. For $\gamma > 0$, some fraction of the dust is exposed to starlight intensities $U \gtrsim 10$, and the fraction of the total power that enters the 24 μm band increases. For the particular size distributions that have been adopted for these models (see Figure 11), the models with $q_{\text{PAH}} = 0.47\%$ and 4.6% (Figures 19a,b differ by only a factor ~ 1.5 in $(\nu L_{\nu})_{24}/L_{\text{TIR}}$ in the single-photon heating limit ($U_{\text{min}} < 1$, $\gamma = 0$).

The emission into the 7.9 μm band is a different story. Figures 19c,d show that in the single-photon heating limit, the fraction of the power radiated into the 7.9 μm band is essentially proportional to q_{PAH} : as q_{PAH} increases from 0.47% to 4.6%, $(\nu L_{\nu})_{7.9}/L_{\text{TIR}}$ increases from 0.02 to 0.2. As γ is increased, some additional 7.9 μm emission is produced; this results in a noticeable fractional increase for the $q_{\text{PAH}} = 0.47\%$ model, but for the $q_{\text{PAH}} = 4.6\%$ model the additional emission produces a very small fractional change in $\langle \nu L_{\nu} \rangle_{7.9}/L_{\text{TIR}}$, which remains dominated by single-photon heating.

To determine q_{PAH} , U_{min} , γ , and M_{dust} , the best procedure is to vary all the parameters to find the dust model which comes closest to reproducing the photometry. This procedure is used by Draine et al. (2006) in their study of the dust properties of the SINGS galaxy sample.

However, it is also possible to use a graphical procedure to find values of q_{PAH} , U_{min} , and γ that are consistent with the observed data. We assume that we have Spitzer photometry in 5 bands: the 3.6 μm and 7.9 μm bands of IRAC, and the 24, 71, and 160 μm bands of MIPS. The 3.6 μm band observations are used with eq. (24) and (25) to obtain $\langle F_{\nu}^{\text{ns}} \rangle_{7.9}$ and $\langle F_{\nu}^{\text{ns}} \rangle_{24}$. We define three ratios of observables:

$$P_{7.9} \equiv \frac{\langle \nu F_{\nu}^{\text{ns}} \rangle_{7.9}}{\langle \nu F_{\nu} \rangle_{71} + \langle \nu F_{\nu} \rangle_{160}} \quad , \quad (26)$$

$$P_{24} \equiv \frac{\langle \nu F_{\nu}^{\text{ns}} \rangle_{24}}{\langle \nu F_{\nu} \rangle_{71} + \langle \nu F_{\nu} \rangle_{160}} \quad , \quad (27)$$

$$R_{71} \equiv \frac{\langle \nu F_\nu \rangle_{71}}{\langle \nu F_\nu \rangle_{160}} . \quad (28)$$

For starlight intensities $0.1 \lesssim U \lesssim 10^2$, the bulk of the power radiated by dust emerges in the 50–200 μm wavelength range, and therefore the total dust luminosity is approximately proportional to $[\langle \nu F_\nu \rangle_{71} + \langle \nu F_\nu \rangle_{160}]$. The ratio R_{71} is sensitive to the temperature of the $a \gtrsim 0.01 \mu\text{m}$ grains that dominate the far-infrared emission; R_{71} is therefore an indicator for the intensity of the starlight heating the dust.

9.1. Determining the PAH Fraction q_{PAH}

$P_{7.9}$ is proportional to the fraction of the dust power radiated in the PAH features. Because the 7.9 μm emission is almost entirely the result of single-photon heating, $P_{7.9}$ depends very weakly on the starlight intensity.

Figure 20 shows $P_{7.9}$ vs. R_{71} for a sequence of grain models, each with a different PAH abundance q_{PAH} . The model with the lowest value of q_{PAH} naturally has very low values of $P_{7.9}$. Because of the very low PAH abundance in Figure 20a, a very small amount of dust exposed to high values of U can enhance the 8 μm emission, and therefore $P_{7.9}$ increases notably as γ increases from 0, with increasing amounts of dust exposed to radiation intensities between U_{min} and $U_{\text{max}} = 10^6$. However, as q_{PAH} is increased, $P_{7.9}$ becomes less sensitive to γ , because single-photon heating of the PAHs produces 7.9 μm emission even when U is small.

Based on modeling many spectra, we expect that the 7.9 μm emission will primarily arise from single-photon heating, i.e., $P_{7.9}$ will be close to the value calculated for $\gamma = 0$. The approximate value of q_{PAH} can therefore be determined by finding a dust model among Figures 20a-g for which the observed $(R_{71}, P_{7.9})$ point falls just above the $\gamma = 0$ curve. The location $(R_{71}, P_{7.9})$ on the appropriate plot also gives an estimate for U_{min} and γ , but these parameters are better determined using the 24 μm emission, as described below.

9.2. Determining U_{min} and γ

P_{24} is proportional to the fraction of the dust power radiated near 24 μm . As seen in Figure 7, 24 μm emission can be produced by single-photon heating of $a \approx 15 - 40 \text{ \AA}$ grains. For a given dust model there is therefore a limiting value of P_{24} that applies for $0.1 \lesssim U \lesssim 10$ where the bulk of the dust power is captured in the 71 and 160 μm bands. However, when some fraction of the grains are heated by starlight with intensities $U \gtrsim 20$ (see Figure 15), larger dust grains can be heated sufficiently to add to the 24 μm emission. As a result R_{24} is sensitive to the value of γ .

To estimate the value of γ , one looks for a dust model in Figure 21 with the value of q_{PAH} found from Figure 20. The observed location of (R_{71}, P_{24}) on Fig. 21 then allows U_{min} and γ to be

determined. It may happen that (U_{\min}, γ) estimated from Figure 21 differs from (U_{\min}, γ) indicated by Figure 20. When this occurs, it is an indication that a single dust model does not perfectly reproduce the observed 7.9/24/71/160 μm colors. We recommend using the values of (U_{\min}, γ) estimated from Figure 21 as they are less sensitive to the adopted value of q_{PAH} .

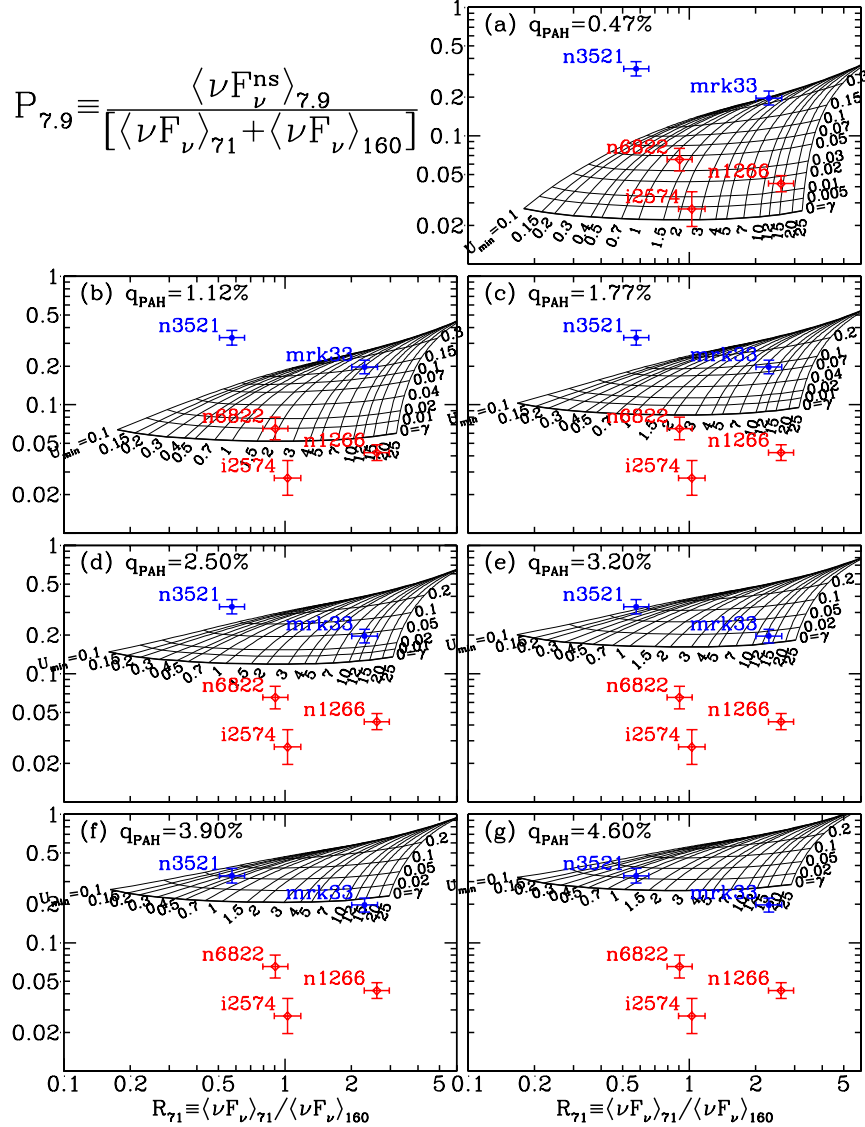


Fig. 20.— IRAC 7.9 μm power relative to MIPS 71 and 160 μm power versus MIPS 71/MIPS 160 band ratio.

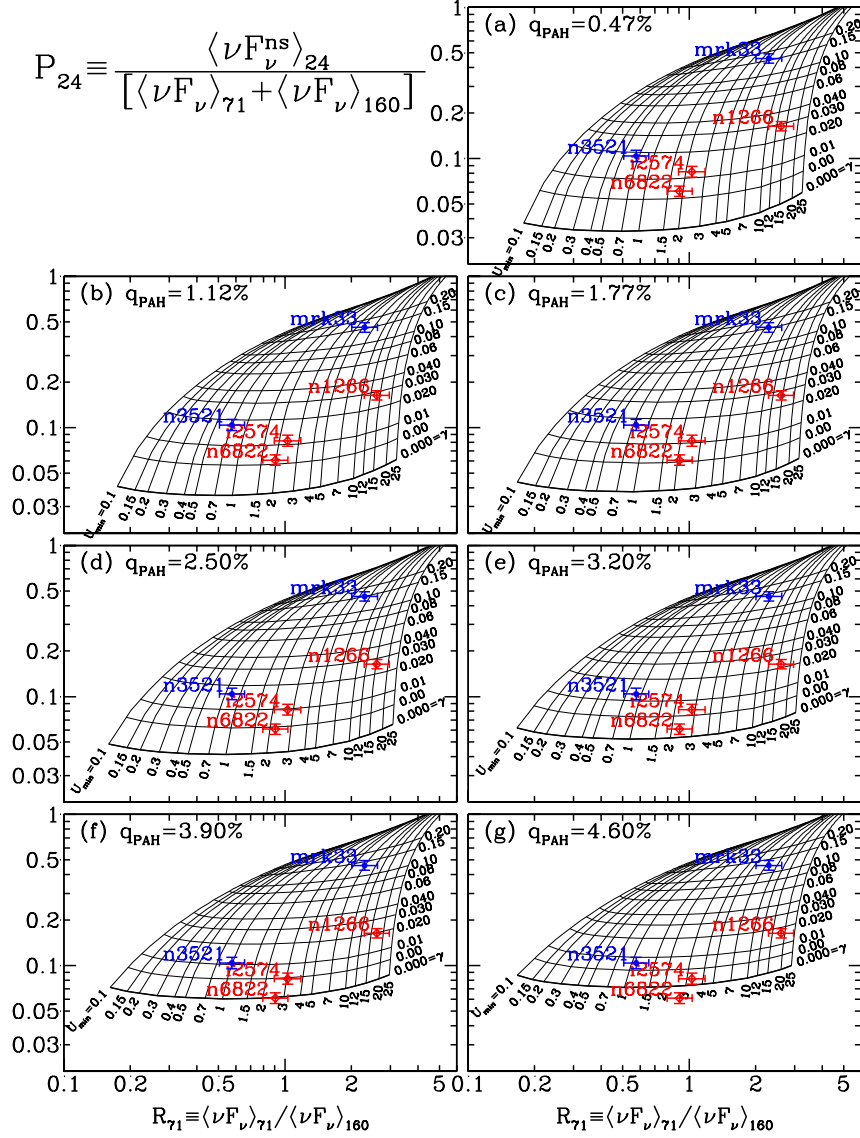


Fig. 21.— MIPS band ratios for models.

9.3. Determining f_{PDR}

Young stars tend to be in or near to dust clouds. In star-forming galaxies such as the Milky Way, we expect that a significant fraction of the starlight emitted by O and B stars will be absorbed by dust that happens to be relatively close to the star, so that the starlight intensity is significantly above the average starlight intensity. Photodissociation regions (PDRs) are typical examples of such environments.

For the power-law distribution of starlight intensities given by eq. (23), we can calculate a

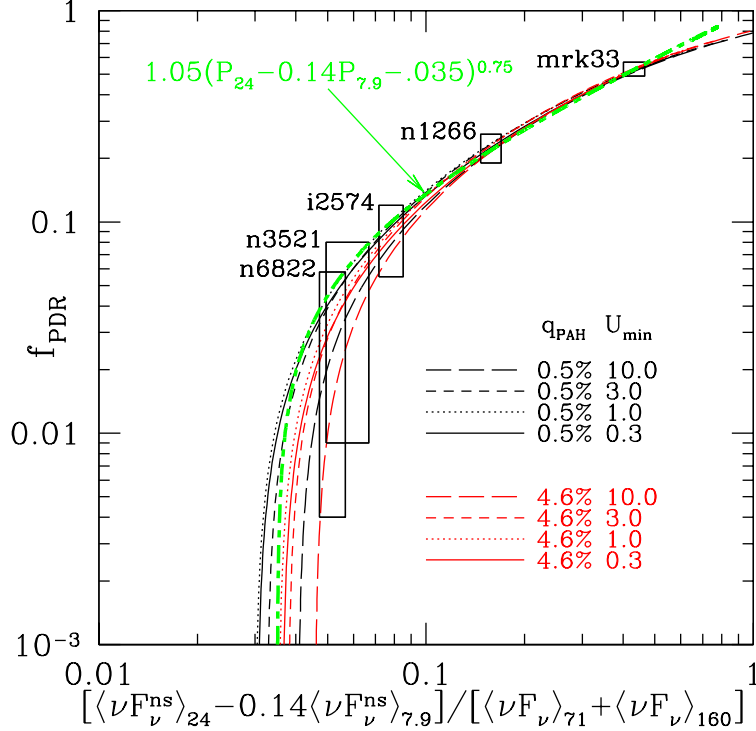


Fig. 22.— f_{PDR} , the fraction of the dust infrared luminosity radiated by dust grains in regions where $U > 10^2$, plotted as a function of the observable $(P_{24} - 0.14P_{7.9})$. For the 5 example galaxies, the width of the rectangle corresponds to the $\pm 1\sigma$ uncertainty in $P_{24} - 0.14P_{7.9}$. The fitting function $1.05(P_{24} - 0.14P_{7.9} - 0.035)^{0.75}$ approximates the model results.

quantity f_{PDR} , which we define here as the fraction of the total dust luminosity that is radiated by dust grains in regions where $U > 10^2$:

$$f_{\text{PDR}} = \frac{\gamma \ln(U_{\text{max}}/10^2)}{(1 - \gamma)(1 - U_{\text{min}}/U_{\text{max}}) + \gamma \ln(U_{\text{max}}/U_{\text{min}})} \quad (29)$$

If U_{min} and γ are known (e.g., either determined by finding the best-fit $(q_{\text{PAH}}, U_{\text{min}}, \gamma)$ from the 3-dimensional model space, or by following the graphical procedures described above), f_{PDR} can be calculated from eq. (29). Here we show how f_{PDR} can be estimated directly from IRAC and MIPS photometry.

For the Milky Way dust models considered here, PAHs undergoing single-photon heating convert a small fraction of the absorbed starlight power into $24\mu\text{m}$ emission, but when a distribution of starlight intensities is present, there is additional $24\mu\text{m}$ emission from high intensity regions. The $24\mu\text{m}$ contribution from PAHs depends, of course, on the PAH abundance. We find that for our models f_{PDR} can be closely related to the fraction of the power radiated at $24\mu\text{m}$ after subtraction

of the contribution of PAHs to the $24\mu\text{m}$ power. We find that the combination $(P_{24} - 0.14P_{7.9})$ gives a quantity that is sensitive to U and relatively insensitive to the value of q_{PAH} .

Figure 22 shows f_{PDR} versus $P_{24} - 0.14P_{7.9}$ for eight different dust models with different values of q_{PAH} and U_{min} . We see that the curves fall within a narrow band. For these dust models, f_{PDR} can be estimated from the observable $P_{24} - 0.14P_{7.9}$ using Figure 22.

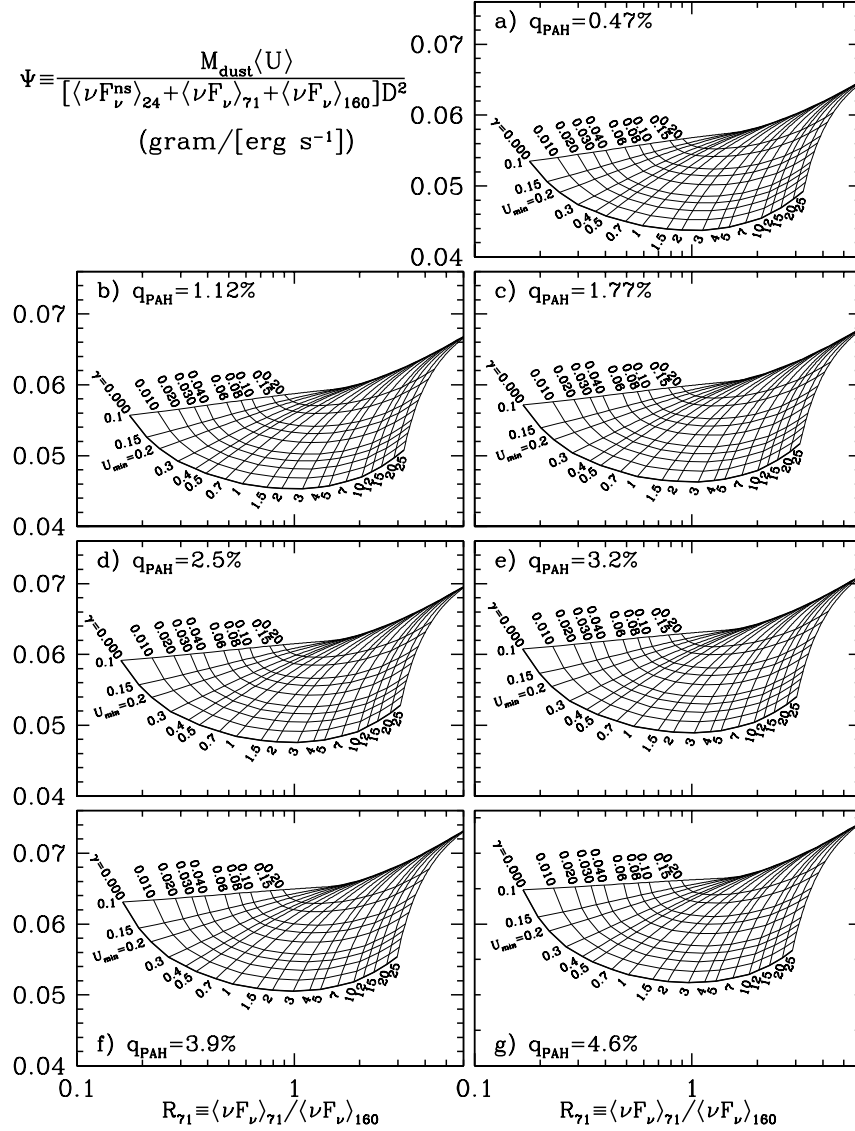


Fig. 23.— Value of Ψ for dust mass estimation (see text).

9.4. Examples

Table 7: Galaxy Examples.

	IC2574	Mark 33	NGC 1266	NGC 3521	NGC 6822
D (Mpc)	4.02	21.7	31.3	9.0	0.49
$\langle F_\nu \rangle_{3.6}$ (Jy) ^a	0.156 ± 0.016	0.027 ± 0.003	0.056 ± 0.006	2.12 ± 0.21	2.20 ± 0.22
$\langle F_\nu \rangle_{7.9}$ (Jy) ^a	0.066 ± 0.007	0.125 ± 0.013	0.087 ± 0.009	6.23 ± 0.62	1.41 ± 0.14
$\langle F_\nu \rangle_{24}$ (Jy) ^a	0.278 ± 0.013	0.836 ± 0.034	0.861 ± 0.035	5.47 ± 0.22	2.59 ± 0.10
$\langle F_\nu \rangle_{71}$ (Jy) ^a	5.10 ± 0.37	3.82 ± 0.28	11.45 ± 0.80	57.2 ± 4.0	59.2 ± 4.2
$\langle F_\nu \rangle_{160}$ (Jy) ^a	10.8 ± 1.4	3.63 ± 0.46	9.6 ± 1.2	$217. \pm 26$	143 ± 17
$P_{7.9}$.027	0.196	0.0435	0.529	0.065
P_{24}	.0810	0.460	0.168	0.166	0.061
R_{71}	1.08	2.33	2.55	0.582	0.944
q_{PAH} from Fig. 20	0.5%	3.2%	0.5%	4.6%	1.1%
U_{min} from Fig. 21	2.3	7	12.5	1.1	2
γ from Fig. 21	0.012	0.14	0.029	0.007	0.006
$\langle U \rangle$ (from eq. 33)	2.6	18.	16.	1.2	2.1
Ψ (g/(ergs s ⁻¹))	0.046	0.061	.049	0.054	0.0465
$\log_{10}(M_{\text{dust}}/M_{\odot})$	5.79	6.41	7.04	8.10	5.15

^a Dale et al. (2006)

To illustrate this, five galaxies are indicated in Figures 20 and 21: NGC 1266, NGC 3521, NGC 6822, IC 2574, and Markarian 33. Table 7 gives the measured global fluxes for these galaxies (Dale et al. 2005), the derived ratios $P_{7.9}$, P_{24} , and R_{71} , and the values of q_{PAH} , U_{min} , and γ obtained from the procedure described in §§9.1,9.2. Below we comment on the individual cases.

IC 2574: In Figure 20, the very low value of $P_{7.9} = 0.027$ only falls on the model grid in Figure 20a, therefore we select $q_{\text{PAH}} = 0.5\%$. From Figure 21a, we find $U_{\text{min}} \approx 2.3$ and $\gamma \approx 0.012$.

Mark 33: From Figure 20e, we estimate $q_{\text{PAH}} \approx 3.2\%$. The very high value of $P_{24} = 0.46$ requires $U_{\text{min}} \approx 7$ and $\gamma \approx 0.14$ on Figure 21e in order to have enough hot dust to reproduce the observed 24 μm flux. The very large value found for γ suggests that a large fraction of the dust heating in Mark 33 is taking place in photodissociation regions near OB associations, consistent with the dwarf starburst nature of this galaxy (Hunt et al. 2005).

NGC 1266: The low value of $P_{7.9} \approx 0.044$ can only be reproduced in Figure 20 by models with small values of q_{PAH} . Of the values of q_{PAH} for which spectra have been computed, $q_{\text{PAH}} = 0.47\%$ is preferred. Turning now to Figure 21a, we find that $U_{\text{min}} \approx 12.5$ and $\gamma \approx 0.029$. The values of q_{PAH} , U_{min} , and γ found by this graphical exercise are in good agreement with the best-fit values of $q_{\text{PAH}} = 0.47\%$, $U_{\text{min}} = 12$, and $\gamma = 0.029$ (Draine et al. 2006).

NGC 3521: From Figure 20g, we find $q_{\text{PAH}} \approx 4.6\%$. From Figure 21g, we obtain $U_{\text{min}} \approx 1.1$ and $\gamma \approx 0.007$. SCUBA fluxes are also available for this galaxy (Dale et al. 2005); when the 850 μm flux is used to constrain the grain model, Draine et al. (2006) find that it is difficult to simultaneously reproduce the MIPS and SCUBA photometry. The overall best fit is found for $U_{\text{min}} = 2$, $\gamma = 0.01$.

NGC 6822: From Figure 20b we estimate $q_{\text{PAH}} = 1.1\%$. From Figure 21g, we estimate $U_{\text{min}} \approx 2.0$ and $\gamma \approx 0.006$. These are in agreement with the best-fit values $q_{\text{PAH}} = 1.2\%$, $U_{\text{min}} = 2.0$, $\gamma = 0.005$ found by Draine et al. (2006).

9.5. Estimating the Dust Mass M_{dust}

Consider a galaxy at distance D . If j_ν is the dust emissivity per H nucleon, then the flux is

$$F_\nu = \frac{M_{\text{H}}}{m_{\text{H}}} \frac{j_\nu}{D^2} \quad , \quad (30)$$

and the dust mass

$$M_{\text{dust}} = \left(\frac{M_{\text{dust}}}{M_{\text{H}}} \right) m_{\text{H}} \frac{F_\nu}{j_\nu} D^2 \quad . \quad (31)$$

If we know the values of $(M_{\text{dust}}/M_{\text{H}})$ and j_ν for a given grain model, we can estimate M_{dust} directly from the distance D and the observed flux F_ν . However, our estimate for j_ν may depend sensitively on our estimates for q_{PAH} , U_{min} , and γ .

A relatively robust approach to dust mass estimation is to note that for a given dust mixture the total dust luminosity is proportional to $M_{\text{dust}} \langle U \rangle$. Define the quantity

$$\Psi(q_{\text{PAH}}, \gamma, U_{\text{min}}) \equiv \left(\frac{M_{\text{dust}}}{M_{\text{H}}} \right) m_{\text{H}} \frac{\langle U \rangle}{[\langle \nu j_\nu \rangle_{24} + \langle \nu j_\nu \rangle_{71} + \langle \nu j_\nu \rangle_{160}]} \quad , \quad (32)$$

where m_{H} is the mass of an H atom, and $\langle U \rangle$ is the mean starlight intensity. For the distribution function (23), with $\alpha = 2$, $\langle U \rangle$ is

$$\langle U \rangle \equiv \frac{\int U dM_{\text{dust}}}{\int dM_{\text{dust}}} = (1 - \gamma)U_{\text{min}} + \frac{\gamma U_{\text{min}} \ln(U_{\text{max}}/U_{\text{min}})}{1 - U_{\text{min}}/U_{\text{max}}} \quad . \quad (33)$$

The dust mass is related to the observed fluxes by

$$M_{\text{dust}} = \frac{\Psi}{\langle U \rangle} [\langle \nu F_\nu \rangle_{24} + \langle \nu F_\nu \rangle_{71} + \langle \nu F_\nu \rangle_{160}] D^2 \quad . \quad (34)$$

For a given dust model, we can calculate Ψ , which is shown in Figures 23(a-g). We observe that the values of Ψ in Figures 23(a-g) range only from 0.044 to $\sim 0.066 \text{ g}/(\text{ergs s}^{-1})$, with $\Psi \approx 0.055 \text{ g}/(\text{ergs s}^{-1})$ as a representative value. However, if we already have estimates for q_{PAH} , U_{min} , and γ , it is straightforward to obtain an accurate value for $\Psi(q_{\text{PAH}}, U_{\text{min}}, \gamma)$ from Figure 23.

To summarize, the procedure for estimating the dust mass M_{dust} is as follows:

1. Use $\langle F_\nu^{\text{ns}} \rangle_{7.9}$, $\langle F_\nu^{\text{ns}} \rangle_{24}$, $\langle F_\nu \rangle_{71}$, and $\langle F_\nu \rangle_{160}$ to calculate $P_{7.9}$, P_{24} , and R_{71} .
2. Use R_{71} and $P_{7.9}$ to estimate q_{PAH} by finding the value of q_{PAH} such that $(R_{71}, P_{7.9})$ falls just above the $\gamma = 0$ curve in Figure 20.

3. Using this value of q_{PAH} , locate (R_{71}, P_{24}) on Figure 21 to determine U_{min} and γ .
4. Using the values of q_{PAH} , U_{min} , and γ , use Figure 23 to find Ψ .
5. Use U_{min} and γ (and $U_{\text{max}} = 10^6$) to calculate $\langle U \rangle$ from eq. (33).
6. Calculate M_{dust} using eq. (34).

We have estimated $\langle U \rangle$, Ψ , and the resulting dust mass M_{dust} for the 5 sample galaxies, with results given in Table 7.

10. Discussion

10.1. Origin of near-IR Continuum Opacity of PAHs

The present models assume that the small-particle end of the grain size distribution is dominated by PAH particles, as assumed by WD01 and Li & Draine (2001b), and the PAH particles are therefore assumed to have a “continuum” component to C_{abs} in order to be able to reproduce 2–6 μm emission seen by ISO (Lu et al. 2003) and emission in the IRAC 4.5 μm filter (Helou et al. 2004). Continuum emission also appears to be present at other wavelengths, e.g., between the 12.6 and 16.45 μm features. In the 2–6 μm wavelength range, even very small carbonaceous grains are arbitrarily taken to have C_{abs} equal to 1% of the continuum that would be produced by free electron absorption in graphite, added to the discrete absorption bands expected for PAHs. The nature of this continuum absorption is unclear. Perhaps some PAHs, e.g., tubular PAHs with appropriate chirality (Zhou et al. 2006) have zero bandgap as in graphite.

We are assuming that the PAHs are responsible for the 2–5 μm continuum. An & Sellgren (2003) find that the 2 μm continuum emission and 3.29 μm PAH emission have different spatial distributions in NGC 7023. Perhaps the 2 μm emission is strongest in regions where the PAHs have been dehydrogenated, thereby suppressing the 3.29 μm emission.

The assumption that the continuum emission originates in PAHs is consistent with the fact that the 9.8 μm and 18 μm silicate features are generally not seen in emission, except from regions (dusty winds, compact H II regions, dust near the Trapezium stars in Orion) where the starlight is thought to be sufficiently intense to heat $a \approx 0.1 \mu\text{m}$ grains to $T \gtrsim 200$ K. However, Li & Draine (2001b) showed that the observed emission from the diffuse interstellar medium in the Milky Way would in fact allow larger amounts of ultrasmall silicate grains than had been estimated previously, because the 9.7 μm silicate emission feature can be “hidden” between the 8.6 μm and 11.3 μm PAH features.

In summary, the origin of the 2–5 μm continuum emission remains uncertain.

10.2. Near-IR Absorption of PAH Ions: Astrophysical Implications

The far-red to near-IR opacity of PAH ions described in Li & Draine (2001a) was derived from earlier experimental data for a small number of small PAH ions [see Salama et al. (1996) and references therein]. More recent laboratory measurements were carried out by Mattioda et al. (2005b) for 27 PAH cations and anions ranging in size from $C_{14}H_{10}$ to $C_{50}H_{22}$. The newly-measured absorption of PAH ions at $0.77\text{--}2.5\ \mu\text{m}$ is considerably higher than previously reported. This further supports our earlier conclusion (Li & Draine 2002b) that visible and near-IR photons are able to excite PAHs to temperatures high enough to emit the mid-IR bands, in agreement with the detection of the PAH features in interstellar regions lacking UV photons (Uchida et al. 1998; Pagani et al. 1999),¹¹ and in agreement with the observation by Sellgren et al. (1990) that the ratio of the IRAS $12\ \mu\text{m}$ emission (to which the PAH features are the dominant contributor) to the total far-IR surface brightness is independent of the effective temperature T_{eff} of the exciting stars, for 24 reflection nebulae for $5000\ \text{K} \leq T_{\text{eff}} \leq 33000\ \text{K}$.

This also relates to our understanding of the origin of interstellar PAHs. At present, the origin and evolution of interstellar PAHs are not very clear. Suggested sources for interstellar PAHs include the injection (into the interstellar medium) of PAHs formed in carbon star outflows (Jura 1987; Latter 1991). However, the PAH emission features are commonly not seen in the mid-IR spectra of C-rich AGB stars. The few C stars which display the PAH features all have a hot companion which emits UV photons (Speck & Barlow 1997; Boersma et al. 2006). It has been suggested that PAHs are present in all C stars but they are simply not excited sufficiently to emit at mid-IR due to lack of UV photons. The new visible-IR cross sections for PAH ions Mattioda et al. (2005b) suggest that PAHs can be excited even by the starlight from a C star, in which case the absence of PAH emission places a limit on the abundance of small PAHs in these outflows.¹²

10.3. Detectability of $6.2\ \mu\text{m}$ Absorption by Interstellar PAHs

The dust model appropriate to Milky Way dust is thought to have $q_{\text{PAH}} \approx 4.6\%$ of the dust mass in PAHs with $N_{\text{C}} < 10^3$ C atoms. The carbonaceous grains with $a < 50\ \text{\AA}$ contain 52 ppm

¹¹ PAH emission features have also been detected in UV-poor dust debris disks around main-sequence stars SAO 206462 [Sp=F8V, $T_{\text{eff}} \approx 6250\ \text{K}$; Coulson & Walther (1995)] and HD 34700 [Sp=G0V, $T_{\text{eff}} \approx 5940\ \text{K}$; Smith et al. (2004b)]. However, in an extensive *Spitzer* IRS spectroscopic survey of 111 T Tauri stars in the Taurus star-forming region, Furlan et al. (2006) found that the PAH emission bands are not seen in dust disks around T Tauri stars of spectral type later than G1.

¹² Jura et al. (2006) reported detection of PAH emission features in HD 233517, an evolved oxygen-rich K2III red giant ($T_{\text{eff}} \approx 4390\ \text{K}$) with circumstellar dust. Jura (2003) argued that the IR excess around HD 233517 is unlikely to be produced by a recent outflow in a stellar wind. Jura et al. (2006) hypothesized that there is a passive, flared disk orbiting HD 233517 and the PAH molecules in the orbiting disk may be synthesized in situ as well as having been incorporated from the ISM.

of C per H nucleon, divided approximately equally between neutral and ionized PAHs. For this model, we predict a $6.22\mu\text{m}$ absorption feature with integrated strength

$$\frac{1}{N_{\text{H}}} \int \Delta\tau \, d\lambda^{-1} = 6.7 \times 10^{-23} \left(\frac{C_{\text{PAH}}/\text{H}}{52 \text{ ppm}} \right) \text{ cm/H} \quad . \quad (35)$$

Chiar & Tielens (2001) found an upper limit $\int \Delta\tau \, d\lambda^{-1} < 0.8 \text{ cm}^{-1}$ toward Cyg OB2 No. 12. For the estimated $N_{\text{H}} = 1.9 \times 10^{22} \text{ cm}^{-2}$, this gives an upper limit

$$\frac{1}{N_{\text{H}}} \int \Delta\tau \, d\lambda^{-1} < 4.2 \times 10^{-23} \text{ cm/H} \quad , \quad (36)$$

somewhat smaller than our estimate (35).

While the present dust model has 52 ppm C in PAHs with $N_{\text{C}} < 5 \times 10^4$, the $6.22\mu\text{m}$ emission is produced mainly by PAHs with $N_{\text{C}} < 500$, which account for only 35 ppm. The $6.2\mu\text{m}$ absorption contributed by PAHs with $N_{\text{C}} < 500$ in our model is consistent with the Chiar & Tielens (2001) upper limit.

The absolute PAH band strengths in Table 1 are only estimates. Because the 3–25 μm emission spectrum for $U = 1$ is almost entirely the result of single-photon heating, the emission spectrum would be almost unaffected if all the PAH band strengths were uniformly reduced by a common factor. However, based on the comparison with theoretical calculations shown in Figure 2, the actual band strengths should be similar in magnitude to the values adopted in Table 1. Spectroscopy of heavily extinguished stars using the IRS instrument on Spitzer Space Telescope should be carried out to attempt to detect the predicted $6.22\mu\text{m}$ absorption from interstellar PAHs.

10.4. Deuterated PAHs

Since the aromatic C–D bond zero-point energy is about 30% lower than that of the C–H bond, H loss is favored over D loss. The PAH D/H ratio might therefore be substantially larger than the total D/H $\approx 2 \times 10^{-5}$ (Allamandola et al. 1989b). The observed sightline-to-sightline variations of (D/H) in interstellar gas have been interpreted as requiring depletion of D by interstellar dust (Linsky et al. 2006). Draine (2004, 2006) has suggested that this depletion of D may take via interactions of PAH ions with the gas, and may imply D/H ≈ 0.3 in interstellar PAHs. Peeters et al. (2004) report tentative detection of emission at 4.4 and $4.65\mu\text{m}$ from deuterated PAHs from the Orion Bar and M17 PDRs. If the emission is in fact due to C–D stretching modes, Peeters et al. (2004) estimate D/H $\approx 0.17 \pm 0.03$ for the emitting PAHs in the Orion Bar and 0.36 ± 0.08 in M17.

Our model for the PAH absorption cross section is based on observed emission spectra, and some of the modeled absorption may be associated with C–D bending modes if interstellar PAHs are appreciably deuterated. Because the observations of 4.4 and $4.65\mu\text{m}$ emission in the Orion Bar and M17 are tentative, we do not attempt here to include any absorption and emission that might result from C–D stretching modes in the $4.5\mu\text{m}$ region.

10.5. Ubiquity and Absence of PAHs in Astrophysical Regions: Rationale for Variable q_{PAH}

The ISO and Spitzer imaging and spectroscopy have revealed that PAHs are a ubiquitous feature of both the Milky Way and external galaxies. Recent discoveries include the detection of PAH emission in a wide range of systems: distant Luminous Infrared Galaxies (LIRGs) with redshift z ranging from 0.1 to 1.2 (Elbaz et al. 2005); distant Ultraluminous Infrared Galaxies (ULIRGs) with redshift $z \sim 2$ (Yan et al. 2005); distant luminous submillimeter galaxies at redshift $z \sim 2.8$ (Lutz et al. 2005); elliptical galaxies with a hostile environment (containing hot gas of temperature $\sim 10^7$ K) where PAHs can be easily destroyed through sputtering by plasma ions (Kaneda et al. 2005); faint tidal dwarf galaxies with metallicity $\sim Z_{\odot}/3$ (Higdon et al. 2006); and galaxy halos (Irwin & Madden 2006; Engelbracht et al. 2006).

However, the PAH features are weak or even absent in low-metallicity galaxies and AGN:

- Based on an analysis of the mid-IR spectra of 60 galaxies obtained by ground-based observations, Roche et al. (1991) reported the lack of PAH emission features in AGN.
- The Small Magellanic Cloud (SMC), an irregular dwarf galaxy with a metallicity just $\sim 1/10$ of solar, exhibits a local minimum at $\sim 12 \mu\text{m}$ in its IR emission spectrum, suggesting the lack of PAHs (Li & Draine 2002c).
- Thuan et al. (1999), Plante & Sauvage (2002), and Houck et al. (2004) have shown that the PAH features are absent in the ISO and Spitzer spectra of SBS 0335-052, a metal-poor ($Z \sim Z_{\odot}/41$) blue compact dwarf galaxy.
- More recently, Hunt et al. (2005), Madden et al. (2006), and Wu et al. (2006) performed a more systematic investigation of the mid-IR spectra of a large number of low-metallicity galaxies (with Z/Z_{\odot} ranging from 0.02 to 0.6) obtained with ISO and Spitzer. They found the PAH features are substantially suppressed in metal-poor dwarf galaxies.
- Using Spitzer IRAC [3.6]–[7.9] colors and *Sloan Digital Sky Survey* (SDSS) [g–r] colors of 313 visible-selected SDSS main sample galaxies, Hogg et al. (2005) found that low-luminosity galaxies show a deficiency in PAH emission, with weak evidence for a dependence of the PAH-to-stellar radiation ratio on metallicity. Rosenberg et al. (2006) performed a similar study for a statistically complete sample of 19 star-forming dwarf galaxies, but they found a significant number of low-luminosity galaxies with very red [3.6]–[7.9] colors, indicating the presence of PAHs (and/or hot dust). They also found that the $7.9 \mu\text{m}$ emission is more strongly correlated with the star formation rate than it is with the metallicity.
- Engelbracht et al. (2005) examined the Spitzer mid-IR colors of 34 galaxies ranging over 2 orders of magnitude in metallicity. They found that the $8 \mu\text{m}$ -to- $24 \mu\text{m}$ color changes abruptly from $F_{\nu}(8\mu\text{m})/F_{\nu}(24\mu\text{m}) \sim 0.7$ for galaxies with $Z/Z_{\odot} > 1/3$ to $F_{\nu}(8\mu\text{m})/F_{\nu}(24\mu\text{m}) \sim 0.08$ for

galaxies with $Z/Z_{\odot} < 1/5$ – $1/3$. They attributed this color shift to a decrease in the $7.7\ \mu\text{m}$ PAH feature at low metallicity.

- The silicate-graphite-PAH model described in this paper has been employed to quantitatively determine the fraction q_{PAH} of the dust mass contributed by PAHs for 61 galaxies in the SINGS survey (Draine et al. 2006). There appears to be a threshold metallicity: galaxies with $[\text{O}/\text{H}] \equiv 12 + \log_{10}(\text{O}/\text{H}) < 8.1$ (i.e., $Z < Z_{\odot}/3$) have $q_{\text{PAH}} < 1.5\%$.

Knowledge of how q_{PAH} varies as a function of galaxy parameters (such as metallicity, luminosity, and morphological type) will have a broad impact –

- It will be essential for properly interpreting the IR cosmological surveys which now often assume a *constant* PAH strength for galaxies [see, e.g., Lagache et al. (2004)].
- It may provide physical insight into the validity of using the line-to-continuum ratio of the $7.7\ \mu\text{m}$ PAH feature as a discriminator between starburst and AGN activity in ULIRGs, i.e., whether the dominant luminosity source of ULIRGs is an AGN or a starburst; see Genzel et al. (1998).
- As local analogs of early galaxies at high redshift which must have formed at very low metallicity, nearby low metallicity systems can provide insight into the early stages of galaxy evolution. The low PAH abundances observed in these galaxies reflect the balance of PAH formation and destruction, and thereby is a valuable probe of the physical conditions following the onset of star formation in primordial gas.
- By comparing with the star-formation rates derived from other tracers, it will allow us to quantitatively evaluate the validity of using the IRAC $8\ \mu\text{m}$ photometry as a reliable tracer for star-formation rates. It is generally believed that the IRAC $8\ \mu\text{m}$ flux is stronger in regions with stronger star-forming activities; however, observations suggest that PAHs are destroyed in star-forming regions with very strong and hard radiation fields (Contursi et al. 2000; Förster Schreiber et al. 2004; Beirão et al. 2006).

10.6. Diversity of PAH Emission Spectra

The PAH absorption and emission properties presented in this series of papers are for “astronomical” PAHs – we fix the peak wavelength and bandwidth of each PAH band to what is observed in most astronomical regions. The strength of each PAH band (on a per carbon or hydrogen atom basis) is also fixed for a specific charge state to be consistent with what is observed in space, measured in the laboratory, or calculated theoretically.

However, there exist variations in the central wavelength, bandwidth and strength of PAH emission bands among different astronomical objects or among different locations within one object:

- Cohen et al. (1989) reported that the central wavelength of the $7.7\ \mu\text{m}$ band varies among different types of objects: it shifts from shorter wavelengths for objects with heavily processed PAHs (e.g. HII regions, reflection nebulae) to longer wavelengths for objects with freshly created PAHs (e.g. planetary nebulae). This wavelength shift has been confirmed by high resolution spectroscopy obtained with the ISO Short Wavelength Spectrometer (Peeters et al. 2002). Similar shifts have also been seen in other bands [e.g. see van Diedenhoven et al. (2004)]. More recently, Bregman & Temi (2005) observed a progressive blueshift in the central wavelength of the $7.7\ \mu\text{m}$ band within 3 reflection nebulae from the edge of the nebulae to places closer to the exciting stars.
- Uchida et al. (2000) reported a progressive broadening of the FWHM of the $7.7\ \mu\text{m}$ band moving toward the exciting star in the reflection nebula vdB 17. This broadening has also been reported for the reflection nebula Ced 21 (Cesarsky et al. 2000). But such a broadening has not been seen in other PAH bands.
- Roelfsema et al. (1996) reported that the $8.6\ \mu\text{m}$ band of the compact HII region IRAS 18434-0242 is almost twice as strong as the $7.7\ \mu\text{m}$ band, while for most objects the $7.7\ \mu\text{m}$ band is stronger than the $8.6\ \mu\text{m}$ band by a factor of $\sim 5-10$.
- Reach et al. (2000) reported that the $11.3\ \mu\text{m}/7.7\ \mu\text{m}$ band ratio of the PAH emission spectrum of the quiescent molecular cloud SMC B1 No. 1 in the SMC is much higher than that of any other Galactic or extragalactic objects. (see Figs. 16 and 17 of Draine & Li (2001)).

While the band-ratio variations can presumably be accounted for by the combined effects of variations in the radiation exciting the PAHs and variations in PAH sizes and ionization state (small PAHs emit more strongly at the 6.2 , 7.7 , $8.6\ \mu\text{m}$ bands, while relatively large PAHs emit more strongly at the $11.3\ \mu\text{m}$ band; neutral PAHs are much stronger $3.3\ \mu\text{m}$ and $11.3\ \mu\text{m}$ emitters and weaker 6.2 , 7.7 and $8.6\ \mu\text{m}$ emitters compared to their charged counterparts), we do not intend to confront our PAH model with extreme spectral variations, such as the observed spectrum of IRAS 18434-024 (with the $8.6\ \mu\text{m}$ band almost twice as strong as the $7.7\ \mu\text{m}$ band) which, according to Roelfsema et al. (1996), is possibly rich in non-compact PAHs. Because of the way we design the “astronomical” PAH model, the present model is not able to account for the central wavelength shifts and the $7.7\ \mu\text{m}$ band broadening, although experimental investigations have been carried out [e.g. see Hudgins & Allamandola (1999)].

Hudgins & Allamandola (2005) discuss recent work toward PAH identification, with attention to the effects of N substitution. Future, more realistic modeling will require more extensive knowledge of PAH properties than is now available from laboratory studies [e.g., Hudgins & Allamandola (1999); Mattioda et al. (2005b,a)] and theoretical calculations [e.g., Bakes et al. (2001a,b); Mallocci et al. (2004); Mulas et al. (2006); Mallocci et al. (2006)].

10.7. Other Grain Models

The dust model used in this study is, of course, provisional. The model assumes the amorphous silicate and carbonaceous material to be in physically separate grains. While this appears to be consistent with observations, including the observed absence of polarization in the $3.4\mu\text{m}$ absorption feature (Chiar et al. 2006), it is by no means observationally established.

Our models have also used the dielectric tensor of crystalline graphite to estimate the infrared absorption by carbonaceous grains with $a \gtrsim 0.01\mu\text{m}$. Some form of amorphous carbon may provide a better approximation for interstellar carbonaceous material that may be formed from agglomeration of PAHs followed by cross-linking due to ultraviolet photolysis and cosmic ray exposure. The main effect on the present models would be to do away with the broad absorption feature near $30\mu\text{m}$ that appears in the calculated $C_{\text{abs}}(\lambda)$ for graphitic material, as seen in Figure 3, and the corresponding broad emission feature near $30\mu\text{m}$ when the starlight intensity is high enough to heat $a \gtrsim 0.01\mu\text{m}$ carbonaceous grains to $T \gtrsim 10^2$ K.

In this work we focus on the silicate-graphite-PAH model. For other dust models, if they are tailored to reproduce the Milky Way interstellar extinction *and* albedo in the optical/UV *and* meanwhile satisfy plausible interstellar abundance constraints, the derived parameters $M_{\text{dust}}\langle U \rangle$ will be nearly the same as derived from the silicate-graphite-PAH model, simply from energy balance considerations: the energy emitted in the IR must be absorbed by the same dust in the optical/UV. If the dust model reproduces the observed far-infrared emission spectrum of Milky Way dust for $U \approx 1$, then the temperatures of the larger dust grains will scale with changes in U in a manner similar to the present model, and therefore the inferred properties of the radiation field (U_{min}, γ) will presumably be similar.

However, the composite model will probably have a lower optical/UV albedo than observed (Dwek 1997). Because the extinction per H atom is fixed by observations, the lower albedo will result in more total far-infrared emission per H nucleon. Given the uncertainties regarding both the intensity of interstellar starlight and the far infrared emission from dust, composite grain models must be considered to be viable. Additional observational tests to distinguish between dust models are needed.

11. Summary

The principal results of this study are as follows:

1. The wavelength dependence of absorption by interstellar PAHs has been revised to better reproduce observed emission spectra. The adopted $C_{\text{abs}}(\lambda)$ are generally consistent with measured or calculated absorption cross sections for PAHs (Figure 2).
2. Temperature distribution functions have been calculated for PAHs of different sizes, heated

by starlight with the spectrum estimated for the local interstellar radiation field. These temperature distribution functions have been used to compute the time-averaged emission spectra for PAHs of different sizes (Figure 5).

3. Figures 6 and 7 show the efficiency with which PAHs radiate absorbed energy into different emission features. The strong $7.7\ \mu\text{m}$ feature is radiated efficiently only by PAHs with $N_C \lesssim 10^3$ carbon atoms – larger PAHs radiate primarily at longer wavelengths.
4. Emission spectra have been calculated for dust models that reproduce the average Milky Way extinction, using size distributions with different abundances of small PAHs (see Fig. 12).
5. Emission spectra have been calculated for dust mixtures heated by different starlight intensities (see Fig. 13).
6. The dust model used in this paper is found to be in good agreement with observed IRAC $3.6\ \mu\text{m}$ /IRAC $7.9\ \mu\text{m}$ and IRAC $5.7\ \mu\text{m}$ /IRAC $7.9\ \mu\text{m}$ band ratios (see Fig. 16), but underpredicts the observed IRAC $4.5\ \mu\text{m}$ /IRAC $7.9\ \mu\text{m}$ ratio by about a factor 1.5.
7. The far-infrared and submm emission spectrum calculated for the present model appears to be in good agreement with the observed emission from dust in the local Milky Way (see Figure 14).
8. A prescription (eq. 17) is found that allows the total IR emission to be estimated from observed fluxes in the IRAC $7.9\ \mu\text{m}$ band and the 3 MIPS bands. For dust heated by starlight intensities $0.1 < U \lesssim 10^2$, eq. (17) is accurate to within $\sim 10\%$.
9. Emission spectra have been calculated for dust mixtures heated by power-law distributions of starlight intensities (see Fig. 18).
10. A distribution function (eq. 23) is proposed for representing the distribution of starlight intensities heating dust in a galaxy, or region within a galaxy.
11. Graphical procedures are presented that allow dust model parameters to be found using 3 ratios ($P_{7.9}$, P_{24} , and R_{71}) constructed from fluxes measured in IRAC band 4 and MIPS bands 1–3. The graphs provided here (Figs. 20 and 21) allow model parameters q_{PAH} , U_{min} , and γ to be estimated.
12. The fraction f_{PDR} of the dust infrared emission that is contributed by dust in photodissociation regions with $U > 10^2$ can be estimated from IRAC and MIPS photometry using Figure 22.
13. Using a coefficient Ψ obtained from Figure 23, the total dust mass M_{dust} can be estimated from fluxes in the 3 MIPS bands using eq. (34).

We are grateful to G. Mallocci for making available to us theoretical absorption cross sections for a number of PAHs in advance of publication; to E. Peeters for providing SWS spectra of the Orion Bar, M17, and NGC 7027; to K. Sellgren for providing IRS spectra of NGC 7023; to T. Onaka for providing response functions for Akari; and to A. Poglitsch and M. Griffin for providing response functions for PACS and SPIRE. We thank the referee, G. Clayton, for helpful comments. BTB was supported in part by NSF grant AST-0406883. AL is supported in part by the University of Missouri Summer Research Fellowship, the University of Missouri Research Board, and NASA/Spitzer Theory Programs. We are grateful to R.H. Lupton for availability of the SM graphics program, used extensively in preparation of this paper.

REFERENCES

- Adamson, A. J., Whittet, D. C. B., Chrysostomou, A., Hough, J. H., Aitken, D. K., Wright, G. S., & Roche, P. F. 1999, *ApJ*, 512, 224
- Allamandola, L. J., Bregman, J. D., Sandford, S. A., Tielens, A. G. G. M., Witteborn, F. C., Wooden, D. H., & Rank, D. 1989a, *ApJ*, 345, L59
- Allamandola, L. J., Tielens, A. G. G. M., & Barker, J. R. 1985, *ApJ*, 290, L25
- Allamandola, L. J., Tielens, A. G. G. M., & Barker, J. R. 1989b, *ApJS*, 71, 733
- An, J. H. & Sellgren, K. 2003, *ApJ*, 599, 312
- Asplund, M., Grevesse, N., Sauval, A. J., Allende Prieto, C., & Kiselman, D. 2004, *A&A*, 417, 751
- Bakes, E. L. O., Tielens, A. G. G. M., & Bauschlicher, Jr., C. W. 2001a, *ApJ*, 556, 501
- Bakes, E. L. O., Tielens, A. G. G. M., Bauschlicher, Jr., C. W., Hudgins, D. M., & Allamandola, L. J. 2001b, *ApJ*, 560, 261
- Beintema, D. A., van den Ancker, M. E., Molster, F. J., Waters, L. B. F. M., Tielens, A. G. G. M., Waelkens, C., de Jong, T., de Graauw, T., Justtanont, K., Yamamura, I., Heras, A., Lahuis, F., & Salama, A. 1996, *A&A*, 315, L369
- Beirão, P., Brandl, B. R., Devost, D., Smith, J. D., Hao, L., & Houck, J. R. 2006, *ApJ*, 643, L1
- Boersma, C., Hony, S., & Tielens, A. G. G. M. 2006, *A&A*, 447, 213
- Boulanger, F., Abergel, A., Cesarsky, D., Bernard, J. P., Miville Deschênes, M. A., Verstraete, L., & Reach, W. T. 2000, in *ESA SP-455: ISO Beyond Point Sources: Studies of Extended Infrared Emission*, ed. R. J. Laureijs, K. Leech, & M. F. Kessler, 91–98
- Boulanger, F., Boissel, P., Cesarsky, D., & Ryter, C. 1998, *A&A*, 339, 194

- Bregman, J. & Temi, P. 2005, *ApJ*, 621, 831
- Cartledge, S. I. B., Lauroesch, J. T., Meyer, D. M., & Sofia, U. J. 2006, *ApJ*, 641, 327
- Cesarsky, D., Lequeux, J., Ryter, C., & Gérin, M. 2000, *A&A*, 354, L87
- Chiar, J. E., Adamson, A. J., Whittet, D. C. B., Chrysostomou, A., Hough, J. H., Kerr, T. H., Mason, R. E., Poche, P. F., & Wright, G. 2006, *ApJ*, 651, 268
- Chiar, J. E. & Tielens, A. G. G. M. 2001, *ApJ*, 550, L207
- Cohen, M., Tielens, A. G. G. M., Bregman, J., Witteborn, F. C., Rank, D. M., Allamandola, L. J., Wooden, D., & Jourdain de Muizon, M. 1989, *ApJ*, 341, 246
- Contursi, A., Lequeux, J., Cesarsky, D., Boulanger, F., Rubio, M., Hanus, M., Sauvage, M., Tran, D., Bosma, A., Madden, S., & Vigroux, L. 2000, *A&A*, 362, 310
- Coulson, I. M. & Walther, D. M. 1995, *MNRAS*, 274, 977
- Cunha, K., Hubeny, I., & Lanz, T. 2006, *ApJ*, 647, L143
- Dale, D. A., Bendo, G. J., Engelbracht, C. W., Gordon, K. D., Regan, M. W., Armus, L., Cannon, J. M., Calzetti, D., Draine, B. T., Helou, G., Joseph, R. D., Kennicutt, R. C., Li, A., Murphy, E. J., Roussel, H., Walter, F., Hanson, H. M., Hollenbach, D. J., Jarrett, T. H., Kewley, L. J., Lamanna, C. A., Leitherer, C., Meyer, M. J., Rieke, G. H., Rieke, M. J., Sheth, K., Smith, J. D. T., & Thornley, M. D. 2005, *ApJ*, 633, 857
- Dale, D. A., Gil de Paz, A., Gordon, K. D., Armus, L., Bendo, G. J., Bianchi, L., Boissier, S., Calzetti, D., Engelbracht, C. W., Hanson, H. M., Helou, G., Kennicutt, R., Madore, B. F., Martin, D. C., Meyer, M. J., Murphy, E. J., Regan, M. W., Smith, J. D. T., Sosey, M. L., Thilker, D. A., & etal. 2006, in preparation, 000, 000
- Dale, D. A. & Helou, G. 2002, *ApJ*, 576, 159
- Dale, D. A., Helou, G., Contursi, A., Silbermann, N. A., & Kolhatkar, S. 2001, *ApJ*, 549, 215
- Desert, F.-X., Boulanger, F., & Puget, J. L. 1990, *A&A*, 237, 215
- Draine, B. T. 1994, in *ASP Conf. Ser. 58: The First Symposium on the Infrared Cirrus and Diffuse Interstellar Clouds*, ed. R. M. Cutri & W. B. Latter, 227–241
- Draine, B. T. 2003, *ARA&A*, 41, 241
- Draine, B. T. 2004, in *Origin and Evolution of the Elements*, ed. A. McWilliam & M. Rauch, 317–335
- Draine, B. T. 2006, in *Astronomical Society of the Pacific Conference Series*, ed. G. Sonneborn, H. W. Moos, & B.-G. Andersson, 58–69

- Draine, B. T., Dale, D., Bendo, G., & et. al. 2006, in preparation, 000, 000
- Draine, B. T. & Lee, H. M. 1984, *ApJ*, 285, 89
- Draine, B. T. & Li, A. 2001, *ApJ*, 551, 807
- Duley, W. W. & Williams, D. A. 1981, *MNRAS*, 196, 269
- Dwek, E. 1997, *ApJ*, 484, 779
- Elbaz, D., Le Floch, E., Dole, H., & Marcillac, D. 2005, *A&A*, 434, L1
- Engelbracht, C. W., Gordon, K. D., Rieke, G. H., Werner, M. W., Dale, D. A., & Latter, W. B. 2005, *ApJ*, 628, L29
- Engelbracht, C. W., Kundurthy, P., Gordon, K. D., Rieke, G. H., Kennicutt, R. C., Smith, J.-D. T., Regan, M. W., Makovoz, D., Sosey, M., Draine, B. T., Helou, G., Armus, L., Calzetti, D., Meyer, M., Bendo, G. J., Walter, F., Hollenbach, D., Cannon, J. M., Murphy, E. J., Dale, D. A., Buckalew, B. A., & Sheth, K. 2006, *ApJ*, 642, L127
- Finkbeiner, D. P., Davis, M., & Schlegel, D. J. 1999, *ApJ*, 524, 867
- Flagey, N., Boulanger, F., Verstraete, L., Miville Deschenes, M. A., Noriega Crespo, A., & Reach, W. T. 2006, [arXiv:astro-ph/0604238](https://arxiv.org/abs/astro-ph/0604238)
- Förster Schreiber, N. M., Roussel, H., Sauvage, M., & Charmandaris, V. 2004, *A&A*, 419, 501
- Furlan, E., Hartmann, L., Calvet, N., D'Alessio, P., Franco-Hernández, R., Forrest, W. J., Watson, D. M., Uchida, K. I., Sargent, B., Green, J. D., Keller, L. D., & Herter, T. L. 2006, *ApJS*, 165, 568
- Genzel, R., Lutz, D., Sturm, E., Egami, E., Kunze, D., Moorwood, A. F. M., Rigopoulou, D., Spoon, H. W. W., Sternberg, A., Tacconi-Garman, L. E., Tacconi, L., & Thatte, N. 1998, *ApJ*, 498, 579
- Helou, G., Roussel, H., Appleton, P., Frayer, D., Stolovy, S., Storrie-Lombardi, L., Hurt, R., Lowrance, P., Makovoz, D., Masci, F., Surace, J., Gordon, K. D., Alonso-Herrero, A., Engelbracht, C. W., Misselt, K., Rieke, G., Rieke, M., Willner, S. P., Pahre, M., Ashby, M. L. N., Fazio, G. G., & Smith, H. A. 2004, *ApJS*, 154, 253
- Higdon, S. J., Higdon, J. L., & Marshall, J. 2006, *ApJ*, 640, 768
- Hogg, D. W., Tremonti, C. A., Blanton, M. R., Finkbeiner, D. P., Padmanabhan, N., Quintero, A. D., Schlegel, D. J., & Wherry, N. 2005, *ApJ*, 624, 162
- Houck, J. R., Charmandaris, V., Brandl, B. R., Weedman, D., Herter, T., Armus, L., Soifer, B. T., Bernard-Salas, J., Spoon, H. W. W., Devost, D., & Uchida, K. I. 2004, *ApJS*, 154, 211

- Hudgins, D. M. & Allamandola, L. J. 1999, *ApJ*, 513, L69
- Hudgins, D. M. & Allamandola, L. J. 2005, in *IAU Symposium*, ed. D. C. Lis, G. A. Blake, & E. Herbst, Vol. 231, 443–454
- Hunt, L., Bianchi, S., & Maiolino, R. 2005, *A&A*, 434, 849
- Irwin, J. A. & Madden, S. C. 2006, *A&A*, 445, 123
- Joblin, C., Abergel, A., Bregman, J., D’Hendecourt, L., Heras, A. M., Jourdain de Muizon, M., Pech, C., & Tielens, A. G. G. M. 2000, in *ESA SP-456: ISO Beyond the Peaks: The 2nd ISO Workshop on Analytical Spectroscopy*, ed. A. Salama, M. F. Kessler, K. Leech, & B. Schulz, 49–54
- Jones, A. P. & d’Hendecourt, L. 2000, *A&A*, 355, 1191
- Jones, A. P., Duley, W. W., & Williams, D. A. 1990, *QJRAS*, 31, 567
- Jura, M. 1987, in *NATO ASIC Proc. 191: Polycyclic Aromatic Hydrocarbons and Astrophysics*, ed. A. Leger, L. D’Hendecourt, & N. Boccara, 3–12
- Jura, M. 2003, *ApJ*, 582, 1032
- Jura, M., Bohac, C. J., Sargent, B., Forrest, W. J., Green, J., Watson, D. M., Sloan, G. C., Markwick-Kemper, F., Chen, C. H., & Najita, J. 2006, *ApJ*, 637, L45
- Kahanpää, J., Mattila, K., Lehtinen, K., Leinert, C., & Lemke, D. 2003, *A&A*, 405, 999
- Kaneda, H., Onaka, T., & Sakon, I. 2005, *ApJ*, 632, L83
- Kawada, M., Shibai, H., Kaneda, H., & Nakagawa, T. 2004, in *Optical, Infrared, and Millimeter Space Telescopes*. Edited by Mather, John C. *Proceedings of the SPIE*, Volume 5487, pp. 359–368 (2004)., ed. J. C. Mather, 359–368
- Kim, S.-H., Martin, P. G., & Hendry, P. D. 1994, *ApJ*, 422, 164
- Lagache, G., Dole, H., Puget, J.-L., Pérez-González, P. G., Le Floc’h, E., Rieke, G. H., Papovich, C., Egami, E., Alonso-Herrero, A., Engelbracht, C. W., Gordon, K. D., Misselt, K. A., & Morrison, J. E. 2004, *ApJS*, 154, 112
- Latter, W. B. 1991, *ApJ*, 377, 187
- Leger, A. & Puget, J. L. 1984, *A&A*, 137, L5
- Li, A. 2005, *ApJ*, 622, 965
- Li, A. & Draine, B. T. 2001a, *ApJ*, 554, 778
- . 2001b, *ApJ*, 550, L213

- . 2002a, *ApJ*, 564, 803
- . 2002b, *ApJ*, 572, 232
- . 2002c, *ApJ*, 576, 762
- Li, A. & Greenberg, J. M. 1997, *A&A*, 323, 566
- . 2002, *ApJ*, 577, 789
- Linsky, J. L., Draine, B. T., Moos, H. W., Jenkins, E. B., Wood, B. E., Oliveira, C., Blair, W. P., Friedman, S. D., Gry, C., Knauth, D., Lacour, S., Lehner, N., Redfield, S., Shull, J. M., Sonneborn, G., & Williger, G. 2006, *ApJ*, 647, 1106
- Lu, N., Helou, G., Werner, M. W., Dinerstein, H. L., Dale, D. A., Silbermann, N. A., Malhotra, S., Beichman, C. A., & Jarrett, T. H. 2003, *ApJ*, 588, 199
- Lutz, D., Valiante, E., Sturm, E., Genzel, R., Tacconi, L. J., Lehnert, M. D., Sternberg, A., & Baker, A. J. 2005, *ApJ*, 625, L83
- Madden, S. C., Galliano, F., Jones, A. P., & Sauvage, M. 2006, *A&A*, 446, 877
- Malloci, G., Joblin, C., & Mulas, G. 2006, in preparation, 000, 000
- Malloci, G., Mulas, G., & Joblin, C. 2004, *A&A*, 426, 105
- Mason, R. E., Wright, G. S., Adamson, A., & Pendleton, Y. 2006, *astro-ph/0611374*
- Mathis, J. S. 1996, *ApJ*, 472, 643
- Mathis, J. S., Mezger, P. G., & Panagia, N. 1983, *A&A*, 128, 212
- Mathis, J. S., Ruml, W., & Nordsieck, K. H. 1977, *ApJ*, 217, 425
- Mathis, J. S. & Whiffen, G. 1989, *ApJ*, 341, 808
- Mattioda, A. L., Allamandola, L. J., & Hudgins, D. M. 2005a, *ApJ*, 629, 1183
- Mattioda, A. L., Hudgins, D. M., & Allamandola, L. J. 2005b, *ApJ*, 629, 1188
- Mennella, V., Brucato, J. R., Colangeli, L., & Palumbo, P. 1999, *ApJ*, 524, L71
- Moutou, C., Leger, A., & D'Hendecourt, L. 1996, *A&A*, 310, 297
- Moutou, C., Sellgren, K., Verstraete, L., & Léger, A. 1999, *A&A*, 347, 949
- Mulas, G., Malloci, G., Joblin, C., & Toubanc, D. 2006, *astro-ph/0606264*, 000, 000

- Onaka, T., Fujishiro, N., Ihara, C., Ishihara, D., Ita, Y., Kataza, H., Kim, W., Matsuhara, H., Matsumoto, T., Murakami, H., Sakon, I., Uemizu, K., Ueno, M., Wada, T., & Watarai, H. 2004, in *Optical, Infrared, and Millimeter Space Telescopes*. Edited by Mather, John C. Proceedings of the SPIE, Volume 5487, pp. 338-349 (2004)., ed. J. C. Mather, 338–349
- Onaka, T., Yamamura, I., Tanabe, T., Roellig, T. L., & Yuen, L. 1996, *PASJ*, 48, L59
- Pagani, L., Lequeux, J., Cesarsky, D., Donas, J., Milliard, B., Loinard, L., & Sauvage, M. 1999, *A&A*, 351, 447
- Papoular, R., Ellis, K., Guillois, O., Reynaud, C., & Nenner, I. 1993, *J. Chem. Soc. Faraday Trans*, 89, 2289
- Peeters, E., Allamandola, L. J., Bauschlicher, Jr., C. W., Hudgins, D. M., Sandford, S. A., & Tielens, A. G. G. M. 2004, *ApJ*, 604, 252
- Peeters, E., Hony, S., Van Kerckhoven, C., Tielens, A. G. G. M., Allamandola, L. J., Hudgins, D. M., & Bauschlicher, C. W. 2002, *A&A*, 390, 1089
- Peeters, E., Tielens, A. G. G. M., Boogert, A. C. A., Hayward, T. L., & Allamandola, L. J. 2005, *ApJ*, 620, 774
- Piovan, L., Tantalò, R., & Chiosi, C. 2006, *MNRAS*, 366, 923
- Plante, S. & Sauvage, M. 2002, *AJ*, 124, 1995
- Popescu, C. C., Misiriotis, A., Kylafis, N. D., Tuffs, R. J., & Fischera, J. 2000, *A&A*, 362, 138
- Reach, W. T., Boulanger, F., Contursi, A., & Lequeux, J. 2000, *A&A*, 361, 895
- Roche, P. F., Aitken, D. K., Smith, C. H., & Ward, M. J. 1991, *MNRAS*, 248, 606
- Roelfsema, P. R., Cox, P., Tielens, A. G. G. M., Allamandola, L. J., Baluteau, J.-P., Barlow, M. J., Beintema, D., Boxhoorn, D. R., Cassinelli, J. P., Caux, E., Churchwell, E., Clegg, P. E., de Graauw, T., Heras, A. M., Huygen, R., van der Hucht, K. A., Hudgins, D. M., Kessler, M. F., Lim, T., & Sandford, S. A. 1996, *A&A*, 315, L289
- Rosenberg, J. L., Ashby, M. L. N., Salzer, J. J., & Huang, J.-S. 2006, *ApJ*, 636, 742
- Sakata, A., Wada, S., Onaka, T., & Tokunaga, A. T. 1987, *ApJ*, 320, L63
- Sakon, I., Onaka, T., Ishihara, D., Ootsubo, T., Yamamura, I., Tanabé, T., & Roellig, T. L. 2004, *ApJ*, 609, 203
- Salama, F., Bakes, E. L. O., Allamandola, L. J., & Tielens, A. G. G. M. 1996, *ApJ*, 458, 621
- Sellgren, K., Luan, L., & Werner, M. W. 1990, *ApJ*, 359, 384

- Siebenmorgen, R. & Krügel, E. 1992, *A&A*, 259, 614
- Silva, L., Granato, G. L., Bressan, A., & Danese, L. 1998, *ApJ*, 509
- Smith, J. D. T., Dale, D. A., Armus, L., Draine, B. T., Hollenbach, D. J., Roussel, H., Helou, G., Kennicutt, R. C., Li, A., Bendo, G. J., Calzetti, D., Engelbracht, C. W., Gordon, K. D., Jarrett, T. H., Kewley, L., Leitherer, C., Malhotra, S., Meyer, M. J., Murphy, E. J., Regan, M. W., Rieke, G. H., Rieke, M. J., Thornley, M. D., Walter, F., & Wolfire, M. G. 2004a, *ApJS*, 154, 199
- Smith, J. D. T., Draine, B. T., Dale, D. A., Moustakas, J., Kennicutt, R. C., Helou, G., Armus, L., Roussel, H., Sheth, K., Bendo, G. J., Buckalew, B., Calzetti, D., Engelbracht, C. W., Gordon, K. D., Hollenbach, D. J., Li, A., Malhotra, S., Murphy, E. J., & Walter, F. 2006, *ApJ*, submitted, 000, 000
- Smith, T. L., Clayton, G. C., & Valencic, L. 2004b, *AJ*, 128, 357
- Snow, T. P. 2000, *J. Geophys. Res.*, 105, 10239
- Snow, T. P. & Witt, A. N. 1996, *ApJ*, 468, L65
- Speck, A. K. & Barlow, M. J. 1997, *Ap&SS*, 251, 115
- Tanabe, T., Nakada, Y., Kamijo, F., & Sakata, A. 1983, *PASJ*, 35, 397
- Tanaka, M., Matsumoto, T., Murakami, H., Kawada, M., Noda, M., & Matsuura, S. 1996, *PASJ*, 48, L53
- Thuan, T. X., Sauvage, M., & Madden, S. 1999, *ApJ*, 516, 783
- Tielens, A. G. G. M. 2005, *The Physics and Chemistry of the Interstellar Medium (The Physics and Chemistry of the Interstellar Medium, by A. G. G. M. Tielens, pp. . ISBN 0521826349. Cambridge, UK: Cambridge University Press, 2005.)*
- Tielens, A. G. G. M., Hony, S., van Kerckhoven, C., & Peeters, E. 1999, in *ESA SP-427: The Universe as Seen by ISO*, ed. P. Cox & M. Kessler, 579–587
- Tuffs, R. J., Popescu, C. C., Völk, H. J., Kylafis, N. D., & Dopita, M. A. 2004, *A&A*, 419, 821
- Uchida, K. I., Sellgren, K., & Werner, M. 1998, *ApJ*, 493, L109
- Uchida, K. I., Sellgren, K., Werner, M. W., & Houdashelt, M. L. 2000, *ApJ*, 530, 817
- van Dienenhoven, B., Peeters, E., Van Kerckhoven, C., Hony, S., Hudgins, D. M. and Allamandola, L. J., & Tielens, A. G. G. M. 2004, *ApJ*, 611, 928
- Verstraete, L., Pech, C., Moutou, C., Sellgren, K., Wright, C. M., Giard, M., Léger, A., Timmermann, R., & Drapatz, S. 2001, *A&A*, 372, 981

- Verstraete, L., Puget, J. L., Falgarone, E., Drapatz, S., Wright, C. M., & Timmermann, R. 1996, *A&A*, 315, L337
- Webster, A. 1993, *MNRAS*, 264, 121
- Weingartner, J. C. & Draine, B. T. 2001a, *ApJ*, 548, 296
- . 2001b, *ApJS*, 134, 263
- Werner, M. W., Roellig, T. L., Low, F. J., Rieke, G. H., Rieke, M., Hoffmann, W. F., Young, E., Houck, J. R., Brandl, B., Fazio, G. G., Hora, J. L., Gehrz, R. D., Helou, G., Soifer, B. T., Stauffer, J., Keene, J., Eisenhardt, P., Gallagher, D., Gautier, T. N., Irace, W., Lawrence, C. R., Simmons, L., Van Cleve, J. E., Jura, M., Wright, E. L., & Cruikshank, D. P. 2004a, *ApJS*, 154, 1
- Werner, M. W., Uchida, K. I., Sellgren, K., Marengo, M., Gordon, K. D., Morris, P. W., Houck, J. R., & Stansberry, J. A. 2004b, *ApJS*, 154, 309
- Witt, A. N. & Gordon, K. D. 1996, *ApJ*, 463, 681
- Wu, Y., Charmandaris, V., Hao, L., Brandl, B. R., Bernard-Salas, J., Spoon, H. W. W., & Houck, J. R. 2006, *ApJ*, 639, 157
- Yan, L., Chary, R., Armus, L., Teplitz, H., Helou, G., Frayer, D., Fadda, D., Surace, J., & Choi, P. 2005, *ApJ*, 628, 604
- Zhou, Z., Sfeir, M. Y., Zhang, L., Hybertsen, M. S., Steigerwald, M., & Brus, L. 2006, *ApJ*, 638, L105
- Zubko, V., Dwek, E., & Arendt, R. G. 2004, *ApJS*, 152, 211